SHEARING RESISTANCE OF PHRA WIHAN

SANDSTONE FRACTURES UNDER

CONSTANT MEAN STRESS

Pakpoom Naphudsa

A Thesis Submitted in Partial Fulfillment of the Requirements for the

Degree of Doctor of Philosophy of Engineering in Civil,

Transportation and Geo-resources Engineering

Suranaree University of Technology

Academic Year 2018

กำลังเฉือนของรอยแตกในหินทรายชุดพระวิหารภายใต้ความเค้นเฉลี่ยคงที่

นายภาคภูมิ นาพุดซา

SHEARING RESISTANCE OF PHRA WIHAN SANDSTONE

FRACTURES UNDER CONSTANT MEAN STRESS

Suranaree University of Technology has approved this thesis submitted in partial fulfillment of the requirements for the Degree of Doctor of Philosophy.

Thesis Examining Committee

_____

(Assoc. Prof. Dr. Pornkasem Jongpradist)

Chairperson

_____

(Prof. Dr. Kittitep Fuenkajorn)

Member (Thesis Advisor)

_____

(Asst. Prof. Dr. Akkhapun Wannakomol)

Member

_____

(Asst. Prof. Dr. Prachya Tepnarong)

Member

_____
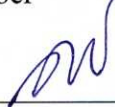
(Asst. Prof. Dr. Decho Phueakphum)

Member

_____ _____

(Prof. Dr. Santi Maensiri) (Assoc. Prof. Flt. Lt. Dr. Kontorn Chamniprasart)

Vice Rector for Academic Affairs Dean of Institute of Engineering

and Internationalization

ภาคภูมิ นาพุดซา : กำลังเฉือนของรอยแตกในหินทรายชุดพระวิหารภายใต้ความเค้นเฉลี่ย
คงที่ (SHEARING RESISTANCE OF PHRA WIHAN SANDSTONE FRACTURES
UNDER CONSTANT MEAN STRESS) อาจารย์ที่ปรึกษา : ศาสตราจารย์ ดร. กิตติเทพ
เฟื่องขจร, 83 หน้า.

การทดสอบกำลังเฉือนแบบสามแกนของรอยแตกได้ดำเนินการกับรอยแตกผิวแบบดึงและ
ผิวเรียบในหินทรายชุดพระวิหารภายใต้สองวิถีความเค้น : ความเค้นล้อมรอบคงที่และความเค้น
เฉลี่ยคงที่ การทดสอบกำลังเฉือนแบบตรงได้ดำเนินการภายใต้ความเค้นตั้งฉากคงที่และความเค้น
เฉือนคงที่ด้วย ผลการทดสอบแสดงให้เห็นว่าภายใต้ความเค้นล้อมรอบต่ำ ทั้งสองวิถีความเค้น
แสดงกำลังเฉือนที่คล้ายคลึงกัน อย่างไรก็ตามภายใต้ความเค้นล้อมรอบสูงกำลังเฉือนสำหรับความ
เค้นเฉลี่ยคงที่ต่ำกว่ากำลังเฉือนของความเค้นล้อมรอบคงที่อย่างชัดเจน กำลังเฉือนของรอยแตกผิว
เรียบไม่ขึ้นกับวิถีความเค้นไม่ว่าความเค้นล้อมรอบใด ภายใต้สภาวะความเค้นตั้งฉากต่ำและไม่มี
ความเค้นล้อมรอบของการทดสอบกำลังเฉือนแบบตรง ผลกระทบของวิถีความเค้นไม่มีนัยยะ
สำคัญ กล่าวได้ว่าความขรุขระของรอยแตกและพฤติกรรมที่ไม่เป็นเส้นตรงของผนังรอยแตกของ
หินภายใต้ความเค้นล้อมรอบสูงเป็นปัจจัยหลักที่ทำให้กำลังเฉือนของรอยแตกขึ้นกับวิถีความเค้น

สาขาวิชา เทคโนโลยีธรณี   ลายมือชื่อนักศึกษา_____
ปีการศึกษา 2561   ลายมือชื่ออาจารย์ที่ปรึกษา_____

PAKPOOM NAPHUDSA : SHEARING RESISTANCE OF PHRA WIHAN

SANDSTONE FRACTURES UNDER CONSTANT MEAN STRESS.

THESIS ADVISOR : PROF. KITTITEP FUENKAJORN, Ph.D., 83 PP.

TRIAXIAL SHEAR TEST/STRESS PATH/DIRECT SHEAR TEST/CONFINEMENT

Triaxial shear tests of fractures has been performed on tension-induced and smooth fractures in Phra Wihan sandstone under two stress paths: constant confining stress and constant mean stress. Direct shear tests are also performed under constant normal stress and constant shear stress. The results show that under low confinement both stress paths show similar shearing resistance. Under high confinement however the shearing resistance for constant mean stress are clearly lower than those of constant confining stress. The shear strengths of smooth fractures are independent of the stress path. Under low normal stress and unconfined condition of the direct shear testing the stress path effect is insignificant. It is postulated that fracture roughness and non-linear behavior of fracture wall rock under high confinements are the main factors that cause stress path dependency of the fracture shear strength.

School of Geotechnology   Student's Signature

Academic Year 2018   Advisor's Signature

ACKNOWLEDGMENTS

Pakpoom Naphudsa

TABLE OF CONTENTS

TABLE OF CONTENTS (Continued)

TABLE OF CONTENTS (Continued)

TABLE OF CONTENTS (Continued)

Page

LIST OF TABLES

LIST OF TABLES (Continued)

LIST OF FIGURES

LIST OF FIGURES (Continued)

LIST OF FIGURES (Continued)

LIST OF FIGURES (Continued)

Figure   **Page**

LIST OF FIGURES (Continued)

Figure   **Page**

SYMBOLS AND ABBREVIATIONS

a	=	Borehole radius
A	=	Empirical constant
A_c	=	Contact area between specimens
B	=	Empirical constant
c	=	Cohesion obtained from rough fracture
C	=	Empirical constant
c_b	=	Cohesion obtained from smooth fracture
D	=	Empirical constant
d_1	=	Axial displacement (monitored in direction of σ_1)
$d_{3,c}$, $d_{o,c}$	=	Calculated lateral displacement induced by d_1 on fracture plane
$d_{3,m}$, $d_{o,m}$	=	Total lateral displacement measured during test
d_n	=	Normal displacement
d_o	=	Lateral displacement (monitored in direction of σ_o)
d_s	=	Shear displacement
E	=	Elastic modulus
G	=	Shear modulus
JCS	=	Joint wall compressive strength
JMC	=	Joint matching coefficient
JRC	=	Joint roughness coefficient
K	=	Bulk modulus
k	=	Ratio of σ_H/σ_v

SYMBOLS AND ABBREVIATIONS (Continued)

L	=	Specimen length (87 mm)
N	=	Normal force
r	=	Radial distance from borehole center
R	=	Shear displacement in unit length
S	=	Shear force
S_r	=	Resisting force
W	=	Specimen width (50 mm)
W_d	=	Distortional strain energy density
$W_{d,f}$	=	Distortional strain energy of fracture at opening wall
W_m	=	Mean strain energy density
z	=	Depth
β	=	Angle between σ_1 and σ_n
ε_1	=	Axial strain
ε_m	=	Mean strain
ε_o	=	Lateral strain (on plane stress)
ε_p	=	Lateral strain (parallel plane stress)
ϕ	=	Friction angle
ϕ_b	=	Basic friction angle
γ_{oct}	=	Octahedral shear strain
μ	=	Plastic deformation vector
σ_1	=	Maximum principal stress (axial stress)
$\sigma_{1,p}$	=	Peak strength in direction of maximum principal stress

SYMBOLS AND ABBREVIATIONS (Continued)

σ_2	=	Intermediate principal stress
σ_3	=	Minimum principal stress
σ_c	=	Unconfined compression strength
σ_H	=	Maximum horizontal principal stress
σ_h	=	Minimum horizontal principal stress
σ_m	=	Mean stress
σ_n	=	Normal stress
σ_o	=	Lateral stress (on plane stress)
σ_p	=	Lateral stress (parallel plane stress)
σ_r	=	Radial principal stress
σ_v	=	vertical principal stress
σ_θ	=	Tangential principal stress
τ	=	Shear stress
τ_{oct}	=	Octahedral shear stress
τ_p	=	Peak shear stress
ψ	=	Angle of σ_θ direction to fracture plane

CHAPTER I

INTRODUCTION

1.1 Background and rationale

Friction and movement of discontinuities in the rock mass are significant factors for stability analysis of engineering structures in rock mass. Their mechanical properties are commonly determined in laboratory. The influences of confinements on the fractures at great depths can be assessed by using triaxial shear test. Direct shear test is performed for on- or near-surface conditions. A significant limitation of these conventional methods is that the mean stress is not constant during the test. There are fundamental differences of the stress paths between laboratory condition and actual in-situ conditions. Near excavation boundaries the radial stress decreases and the tangential stress increases. This leads to a constant mean stress condition. The effect of stress path on the shearing resistance of fractures has rarely been investigated.

1.2 Research objectives

The objectives of this study are to determine the shearing resistance of sandstone fractures by performing triaxial shear and direct shear tests under different stress paths, and to apply strain energy density principle to describe the peak shear strengths and confinements under different stress path conditions.

1.3   Research methodology

The research methodology shown in Figure 1.1 comprises 7 steps; including literature review, sample preparation, laboratory testing, test results and shear strength criteria development, strain energy density of fractures, discussions and conclusions and thesis writing.

1.3.1   Literature review

Literature review is carried out to study the previous researches on stress paths effects on strength rocks, stress paths effects on shear strength of fracture rocks, constant mean stress test, conventional shear tests and strain energy density.
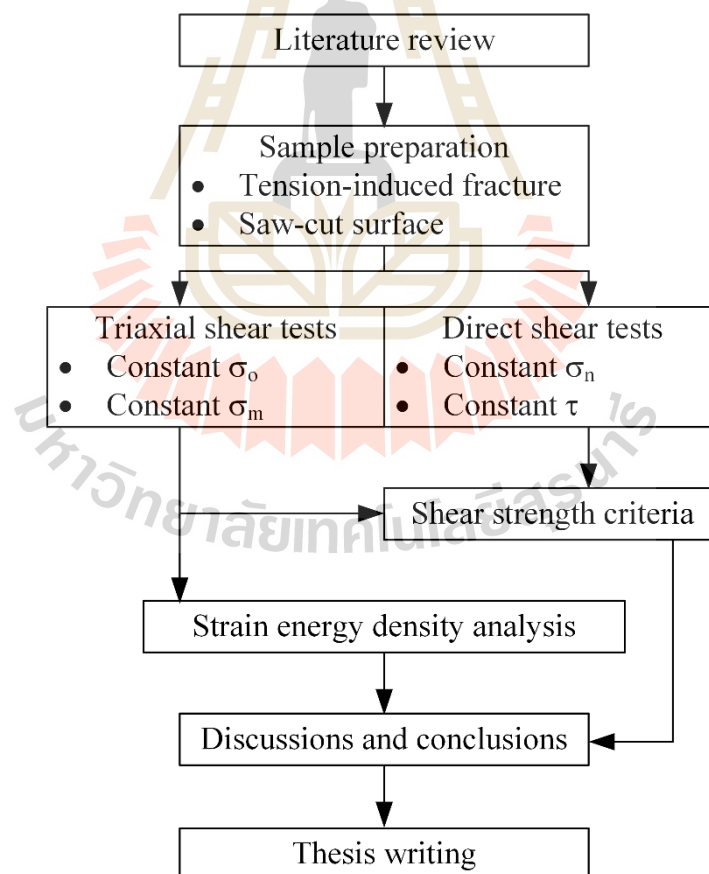
Figure 1.1 Research methodology

The sources of information are from text books, journals, technical reports and conference papers. A summary of the literature review is given in the thesis.

1.3.2 Sample preparation

Sample preparation is carried out in the laboratory at Suranaree University of Technology. Sandstone specimens are obtained from Phra Wihan formation in the northeast of Thailand. They are prepared to obtain rectangular block specimens with nominal dimensions of $50 \times 50 \times 87$ mm^3 for triaxial shear tests and $100 \times 100 \times 180$ mm^3 for direct shear tests. Asperity amplitudes on the fracture are measured from the laser-scanned profiles along the shear direction. They are used to determine the joint roughness coefficient of the tested fractures.

1.3.3 Laboratory testing

The laboratory experiments include the triaxial shear tests and the direct shear tests. They are performed to determine the peak shear strengths and deformations of fractures specimen under the different stress paths.

1.3.4 Test results

Test results from laboratory measurements show in term of major principal stresses (σ_1) corresponding to peak shear strengths as a function of shear displacements, major principal stresses at peak (σ_1) as a function of vertical displacements (d_1), and peak shear strengths (τ) as a function of normal stresses (σ_n). All test results are used to develop the shear strength criteria. Fracture dilations and post-test observations are herein presented.

1.3.5 Strain energy density of fractures

The strain energy density would be more comprehensive than other strength criterion because it considers both stress and stain at failure. The strain energy

density analysis is conducted here assuming that the intact portion of the specimen is rigid and the strain along the fracture strike is equal to zero. The distortion stain energy as a function of mean strain energy are calculated from the principal stresses and strains.

1.3.6 Discussions and conclusions

Discussions are made on reliability and adequacies of the test data. The mechanical properties and behavior of the fractures are compared to previous works. Consummation and application of works are identified.

1.3.7 Thesis writing

All research activities, methods and results are documented and complied in the thesis. The future researches are mentioned in the last part. The research or findings are published in the journals.

1.4 Scope and limitations

The scope and limitations of the research include as follows:

1 Laboratory experiments are conducted on specimens from Phra Wihan sandstone.

2 All tested rough (tension-induced) fractures are artificially made in the laboratory by tension-inducing methods.

3 All tested smooth (saw-cut) fractures are artificially made in the laboratory by a cutting device.

4 Triaxial shear tests

    4.1 All tests are performed using a true triaxial load frame.

    4.2 Triaxial shear tests are performed on all fractures specimens with nominal dimensions of $50 \times 50 \times 87$ mm^3 with the fractures area of

$50{\times}100$ mm^2. Normal stress to fractures plane makes an angle of 60º

with axial stress.

    4.3 Constant confining stresses (σ_o) vary from 1, 3, 7, 12 to 18 MPa

    4.4 Constant mean stresses (σ_m) vary from 20, 25, 30, 35, 40, 45, 50 to 55

MPa.

5   Direct shear tests

    5.1 All tests are performed using a direct shear device (SBEL DR44).

    5.2 Direct shear tests are performed on all fractures specimens with

nominal dimensions of $100{\times}100{\times}160$ mm^3 with the fracture area of

$100{\times}100$ mm^2.

    5.3 Constant normal stresses (σ_n) vary from 1, 2, 3 to 4 MPa.

    5.4 Constant shear stresses (τ) vary from 1, 2, 3 to 4 MPa.

6   Tests are conducted under ambient temperature and dry condition.

7   The research findings are published in an international journal.

1.5   Thesis contents

This research thesis is divided into seven chapters. The first chapter introduces
the thesis by briefly describing the background of problems and significance of the
study. The research objectives, methodology, scope and limitations are identified. The
second chapter presents results of the literature review about stress paths effects on
strength rocks, stress paths effects on shear strength of fracture rocks, constant mean
stress test, conventional shear tests and strain energy density. The third chapter
describes preparation and observation of fractures. The fourth chapter describes the
methodology of shear tests under different stress paths. The test results are used to

develop the shear strength criteria. The post-test of rough fracture is observed in the fifth chapter. Then, the sixth chapter shows the development of strain energy density equation. The seventh chapter provides the discussions, conclusions and recommends the future research studies.
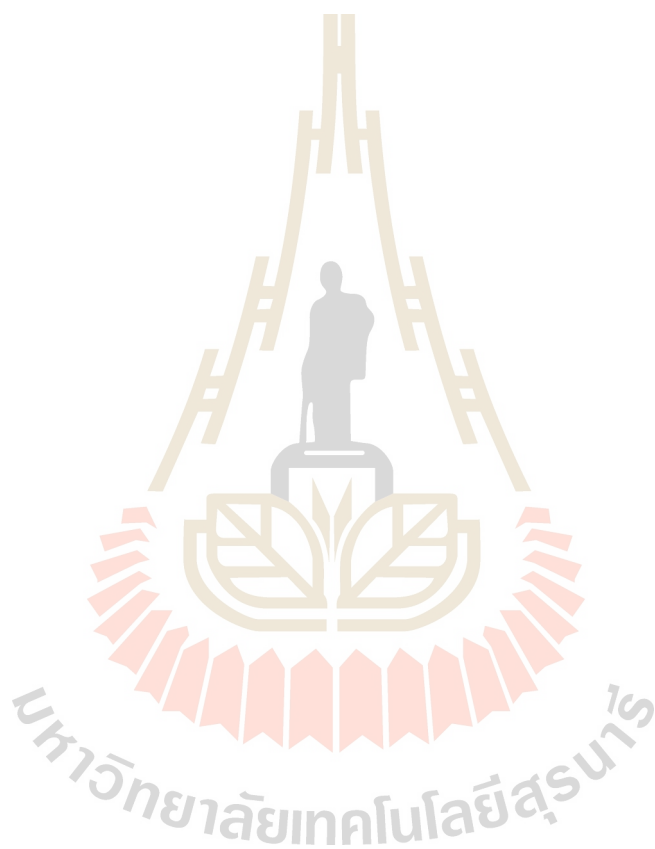
CHAPTER II

LITERATURE REVIEW

2.1   Introduction

Relevant topics and previous research results are reviewed to improve an understanding of the stress paths effects on strength rocks, stress paths effects on shear strength of fracture rocks, constant mean stress tests, conventional shear tests and strain energy density.

2.2   Stress paths effects on strength rocks

In-situ stress is mainly caused by tectonic plates moving and weight of rock above (Hudson et al., 2003). Excavation engineering rotates principal directions and changes the magnitudes of principal stresses around the excavation boundary of unsupported structures. The minimum principal stress (σ_3) is reduced, the intermediate principal stress (σ_2) is unchanged and the maximum principal stress (σ_1) is increased (Zhao and Cai, 2014). The stresses and deformations are evaluated correctly for design supports at depths with safety and economic capital. The complicated in-situ stress path is analyzed using linear elastic compares with stress path for laboratory, as shown in Figure 2.1. This is a fundamental difference from the laboratory testing under monotonic loading condition (Martin, 1997). In the previous works, many researchers investigated the influence of the stress path on strength and deformation of rocks, which two types of stress paths are mainly divided into conventional triaxial compression
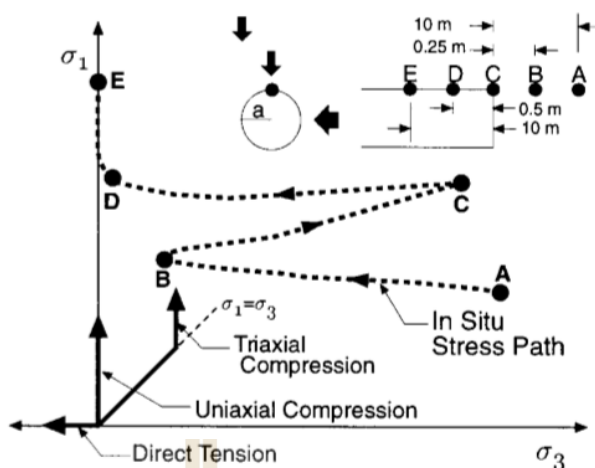
Figure 2.1 Difference between in-situ and laboratory stress paths (Martin, 1997).
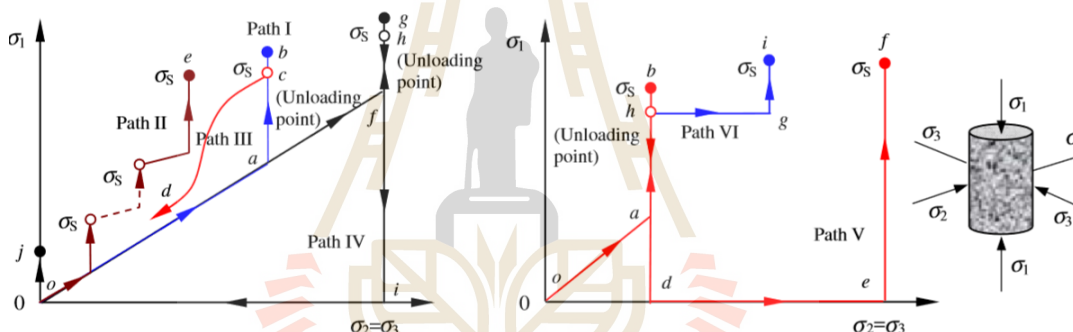
Figure 2.2 Six different loading paths presented in principal stress space (σ_3, σ_1) (Yang et al., 2011).

(Path I) and confining pressure reduction (Path III) (Figure2.2) (Yang et al., 2011). There are contradictory opinions as follow.

1. The strength is independent of stress paths.

Swanson and Brown (1971) investigate the effect of loading path on fracture or strength of rocks. The cylindrical specimens are prepared on Westerly granite and tonalite from Cedar City, Utah. A lesser number of tests are performed on locally located sandstone and white marble. Westerly granite is typical of a hard, good quality

granite and classified as brittle. Cedar city tonalite is much softer. The loading paths

are divided to four types: hydrostatic, constant confining pressure, proportional loading

(the ratio of the axial and radial stress is constant) and uniaxial strain. The tests are

performed by controlling axial strain rate of approximately of 10^{-4} /sec. The strength

of brittle rocks is independent of the stress loading paths, as shown in Figure 2.3. The

sandstone and marble in both brittle and ductile ranges show that they are independent

of the stress loading paths, as shown in Figure 2.4. The results indicate that initiation

of dilatancy and ultimate fracture are independent of the stress paths in stress space.

Crack propagation occurs in apparently brittle rock by action of frictional and geometric

effects of rocks.
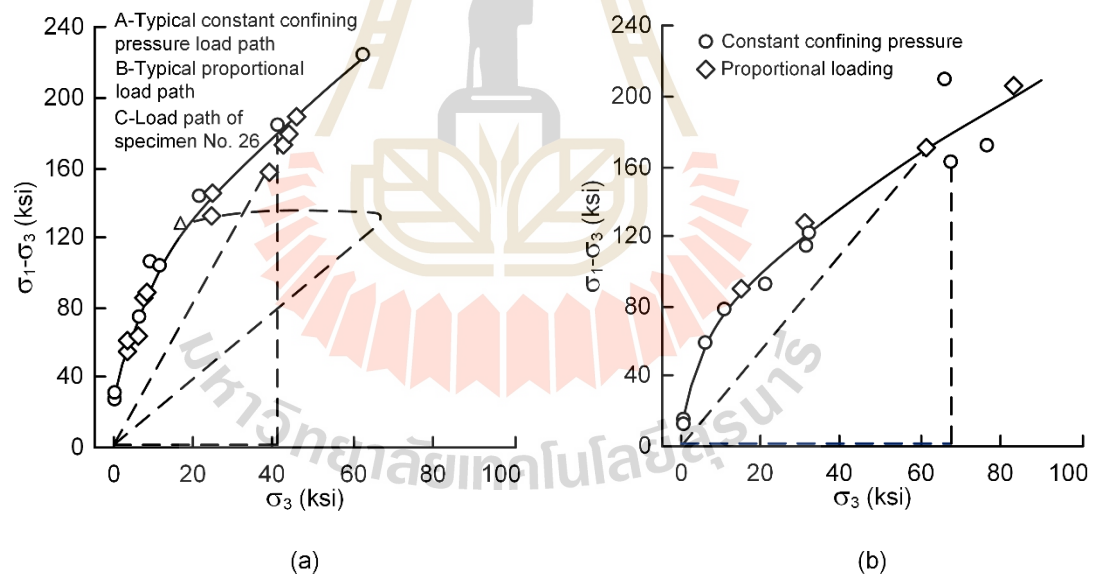
Figure 2.3 Failure locus for Westerly granite (a) and Cedar City tonalite (b) (Modified from Swanson and Brown, 1971).
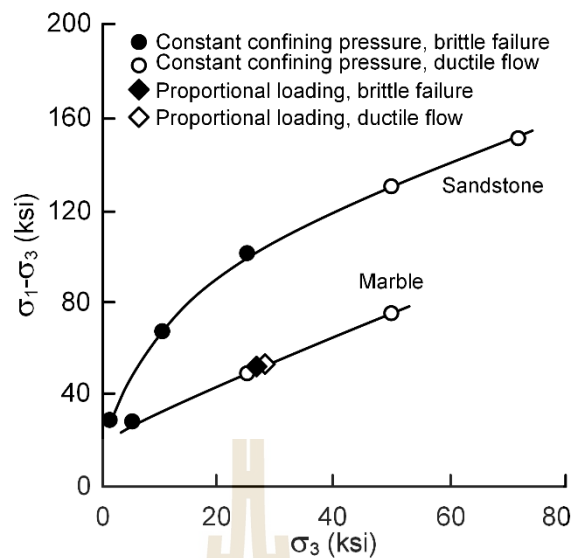
Figure 2.4 Maximum stress difference for sandstone and marble (Modified from Swanson and Brown, 1971).

Crouch (1972) experiments on South African norite by performing with different loading conditions. In the first test, the confining stress is applied initially from 0 to 1000 lb/in^2, at which it is then kept constant as the axial stress is applied until failure occurs. In the second test, the confining stress is decreased from 2000 to 1000 lb/in^2 until failure occurs and then it is increased and decreased in stepwise fashion. During the tests, the confining stress and the axial stress are applied in fixed ratio (proportional loading). The loading paths and results are shown in Figure 2.5. The strength of norite is independent of the manner in axial and confining stresses applied. He states also that a small decrease in confining stress could make a large decrease in axial stress.

Yang et al. (2012) conduct the conventional triaxial compression and reducing confining pressure tests for red sandstone by an MTS815 Flex Test GT rock mechanics experimental system. The triaxial compression test is performed by using a

circumferential displacement rate of 0.06 mm/min until failure. The reducing confining

pressure is performed by the deviatoric stress is applied to predefine (70 or 90% of

triaxial compression) and increased axial at displacement rate of 0.06 mm/min. Then,

the axial stress is constant but the confining stress is reduced at a rate of 0.1 MPa/s until

failure occurred. The results show that the post-peak axial deformation characteristics

of red sandstone changed as the confining pressure is increased from 5 to 65 MPa.

Young's modulus of red sandstone increases nonlinearly with increasing confining

pressure, but Poisson's ratio remains unaffected. The nonlinear Hoek-Brown criterion

shows better peak strength than the linear Mohr Coulomb criterion (Figure2.6). The

residual strength supporting the friction slippage shows a clear linear relationship with

confining pressure which it can be best described using the linear Mohr-Coulomb
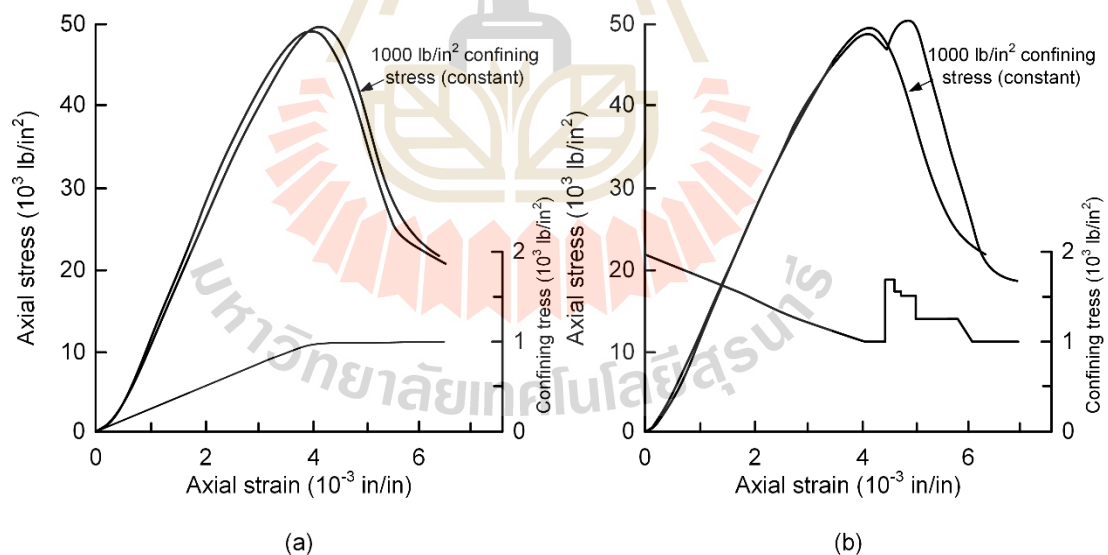
Figure 2.5   Axial stress-axial strain curves for norite under constant confining stress

(a) decrasing and increasing confining stress (b) (Modified from Crouch,

1972).
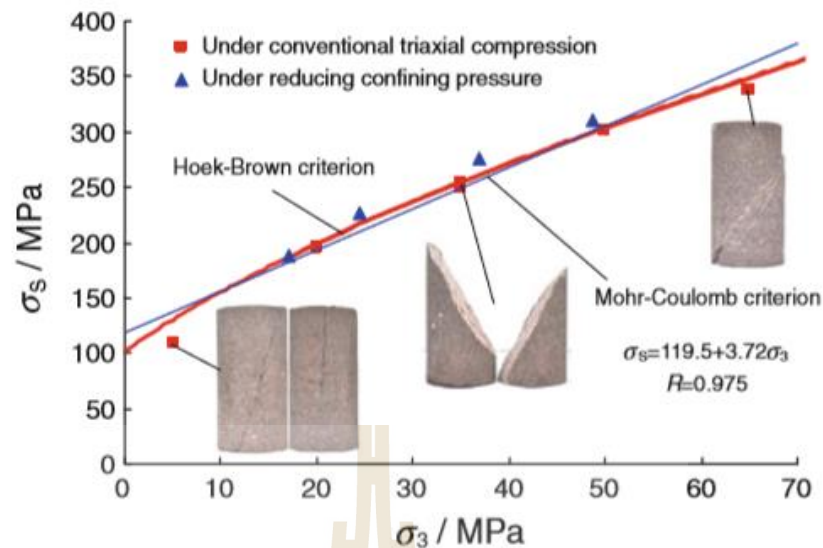
Figure 2.6 Peak strength of red sandstone under different loading paths and criterion (Yang et al., 2012).

criterion (Figure 2.7). It can also be seen that the peak strength and residual strength are not dependent of the loading path. For the conventional triaxial compression tests, the failure mode changed from mixed tension and shear fracture (single shear fracture) to shear fracture with double slippage planes with increasing confining pressure.

    2. Another opinion regard that the stress path has a significant influence on strength and deformation of rocks.

       Jinan gabbro, Changing granite, Yexian marble and Fangshan marble are tested by using the triaxial compression to study the effects of stress paths.

       Path I and III the gabbro shows brittle behavior up to 1.5 kb. Path III the gabbro is more brittle than that in path I of the same stress state. Path I the marble shows brittle behavior below 0.2 kb and when the confining stress about 0.2-0.25 kb the brittle-ductile transition is occurred. However, it is found that some brittle fracture of marble
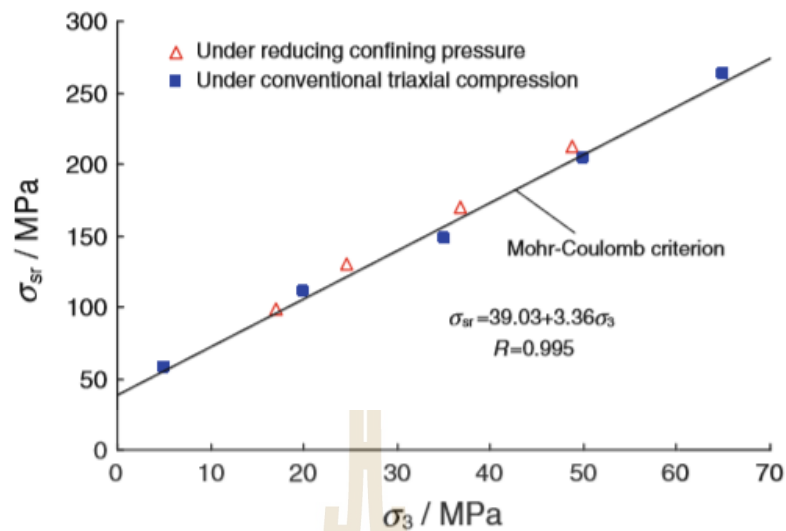
Figure 2.7 Residual strength of red sandstone under different loading paths and criterion (Yang et al., 2012).

could appear in path III, even though confining stress is above 0.25 kb. Ductile behavior appears when the confining stress above 0.25 kb and vanished in ability of sustain loading. These can conclude that the brittleness of rock seems to be related to the stress path (Xiao-xin et al., 1980). The strength of the gabbro and granite in path III is lower than that in path I while the strength of two marbles in path III is higher than in path I (Nai-guang et al., 1981).

Jin-feng et al. (2012) who perform a large scale triaxial test and water effects of the broken limestone. The results show that the dilatancy and shrinkage behavior are related with the stress paths. The shear strength under Path III is slightly lower than that under Path I.

Yang et al. (2011) study the mechanical behavior of coarse marble under different loading paths under triaxial compression. The stress paths I and II are performed by using intact rock. The others are called "flawed sample" that it is to

analyze the re-fracture behavior. The results indicate that the stress path has a significant effect on the strength of coarse marble. The paths I and II are put forward to confirm the strength parameters with linear Mohr-Coulomb criterion, which the value of the path I is lower than that the path II, but the value of internal friction angle of the path I is higher than that the path II. Two loading paths (i.e. Path II by stepping up the confining pressure and Path III by reducing the confining pressure after peak strength) are suggested to confirm the triaxial strengths of rock by one sample that has obvious plastic and ductile deformation. The flawed samples fail with smaller Young's moduli and larger failure strains compares with the intact samples at the same condition.

Hudson and Harrison (2002) state that stress path is defined by the variations of magnitudes and orientations in the three principal stresses. This is unconstrained in term of failure and no significance in an elastic material; however, the stress path has a significance and it is constrained by the failure locus in an inelastic material. If it reaches the failure locus, not only the properties of the materials will change, but the final state will be also different from that based on elasticity. Time is considered to the independent variable for the stress path. In the rock mass it could define that inelastic material, the stress path should be tracked in all analyses of the stress redistribution.

2.3 Stress paths effects on shear strength of fractures rocks

Nai-guang et al. (1987) study frictional sliding of Jinan gabbro and Diancangshan marble by the bishear test method. There are two type of shear stress paths. Case A, the normal stress to the fracture plane is increased first, it is kept constant and then the shear stress is increased until fracture movement occurs. Case B, the normal stress on the fracture plane is increased first and the shear stress is increased to

a certain value, then the shear stress is kept in constancy and the normal stress decreased until the fracture movement occurs. The results indicate that the frictional strength of rocks in case B is higher than that in case A, as shown in Figure 2.8. They conclude that there are two forms of dislocking of the locked fractures: One, the dislocking is occurred by rushing, the fault movement is caused by an increase of the shear stress. The another, the dislocking is occurred by relaxing, the fault movement is caused by a decrease of the normal stress. The form of stick-slip of faults is determined by the path of shear stress change in fault zones (in case A).

Tisa and Kovári (1984) perform a continuous failure state (CFS) of directs shear test which the shear and normal stresses are steadily changed. The stress paths are divided to No.1 and No.2, as shown in Figure 2.9a. No. 1 path start at applied the normal stress of 1 MPa which it is kept constant. The shear stress is applied to reach of 0.43 MPa. After that, the specimen is applied a constant displacement rate as followed the line a. Path No.2 start at applied the normal stress of 4 MPa and the shear stress applied about 2.6 MPa then the normal stress is decreased along the line b. The planar surface is prepared from a granite in a nominal dimension of 15×12 cm. The results shown in Figure 2.9b. The different stress paths have no effect on planar or saw-cut surface. The irregular joint surfaces are prepared from brick with tensile fracture surface and cast cement mortar. The uniaxial compression strength of these are very similar, ranging from 29 MPa for the brick to 32 MPa for the cement mortar. The asperities of the brick are within 2 mm (JRC=8). The shear strength for CFS path agrees well with the conventional test results. These lead to conclude that the shear strengths of those materials tend to be independent to stress paths. The shear displacements are

monitored. The conventional shear test is subjected to large shear displacements until the residual strength is reached.
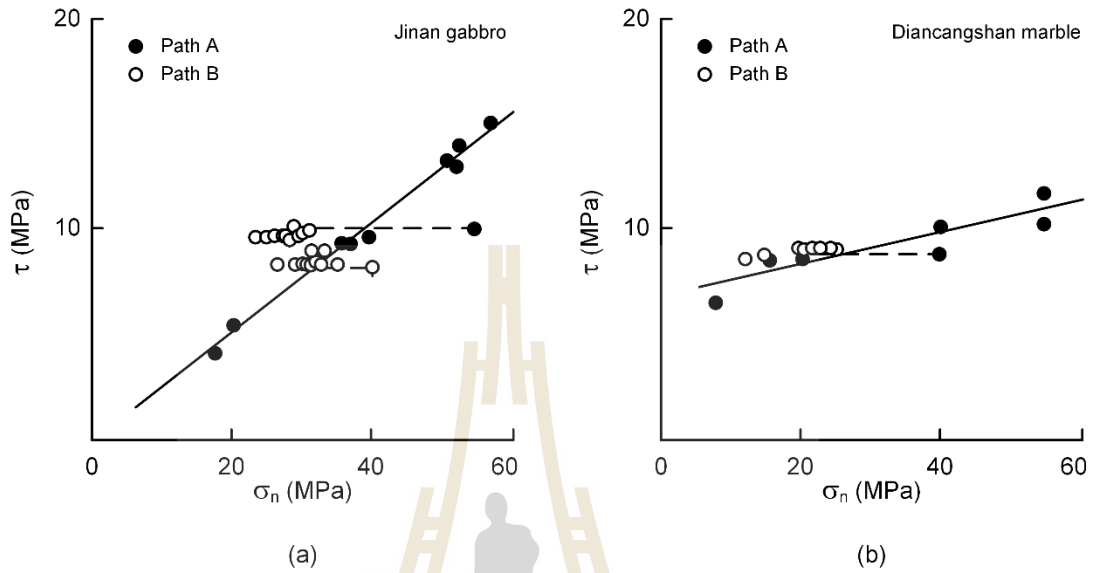
Figure 2.8   Shear stress-normal stress of Jinan gabbro (a) and Diancangshan marble (b) (Modified from Nai-guang et al., 1987).
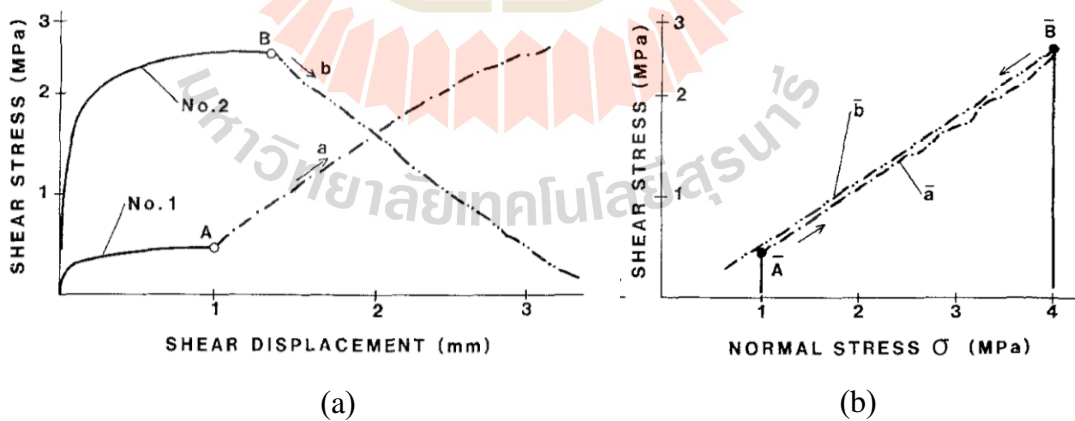
Figure 2.9   Shear stress paths (a) planar surface test results (b) (Modified from Tisa and Kovári, 1984).

Wu et al. (2017) perform friction experiments on a simulated granular gauge using an unload-induced direct-shear (UIDS) model. The saw-cut surface is prepared from the Dark Impala norite. A normal and shear stresses are applied before the test. The stress path of shear testing is designed by the shear stress have been kept constant, during the test, and the normal stress is constantly unloaded at rate of 0.455 MPa/s to induce the frictional slip occurred. The results subject the initial normal stress of 4 MPa and the shear stresses are considered of 0.25, 0.50 and 0.75 MPa (Wu et al., 2014). The test considers the effects of initial shear stress, initial normal stress and unloading rate on the frictional slip. The results show that a greater initial normal stress, a lower shear stress and a larger unloading rate provide the higher strain energy, leading to the higher slip displacement. The excavation caused the deformation of rock mass between opening and fault segment by reducing the normal stress faster than the shear stress. As the results, the decreasing speed of excavation can reduce the probability of induced earthquake occurrence.

2.4 Constant mean stress tests

Kirsch's solution (Brady and Brown, 2004) is used to calculate the stresses and displacements around circular opening which derived from the theory of elasticity. The transformation of the stress is subjected constant means stress which principal radial stress is almost dropped to zero, promptly, tangential stress is increased under mean stress condition.

Kenter et al. (1997) study effects of coring damage by comparing the unconfined strength to constant mean stress paths. Natural sandstones specimens are prepared from a reservoir rock at depth of approximately 3 km. Synthetic sandstones

are created from forming. The results show that the deformations of those are nonlinear and strong component of plasticity. All strengths for the constant mean stress path are higher than the unconfined strength path. The strength of natural specimen for the constant mean stress path is closed to the strength for the unconfined strength of the synthetic sandstones. They indicate that the constant mean stress test can decrease the discrepancy that micro-cracks are generated during coring the specimen.

Mellegard and Pfeifle (1999) perform triaxial compression under constant mean stress. An axisymmetric rock salts are prepared from the Weeks Island in Louisiana. The loading path in function of stress and time is shown in Figure 2.10. The constant mean stress condition, the specimen is applied the loading rate of 0.02 MPa/s until the specimen is under hydrostatic pressure. The new loading path is calculated to decrease the confining pressure until reached zero under the constant rate of 0.02 MPa/s. At the same time, increasing of the axial stress at the rate of 0.04 MPa/s is performed to maintain the constant mean stress. The axial stress is applied continuously until the specimen failed or the confining pressure reached zero. If the confining pressures reach zero, the testing will be stopped because the negative confining stresses are not possible on the testing and the mean stresses are not constant. The results under the constant mean stress path is compared to conventional triaxial compression test, as shown in Figure 2.11. The volumetric strain initially remained zero (no dilation) while deviatoric stress is applied for constant mean stress. For constant confining stress state, the increasing deviatoric stress cause the volumetric strain became negative (dilation). There is no report about elastic moduli because salt rock is inelastic material.

Jeng et al. (2002) study deformational characteristics of Mushan sandstone, experiments with controlled stress paths, including hydrostatic compression, pure

shearing (PS) and conventional triaxial compression paths (CTC). This work focusses
on the short-term behavior (time independent). The cylindrical specimens have a
nominal size of 5.5 cm in diameter and 12.5 cm in height. The load is applied at a rate
of 5 MPa/min. The failure develop of pure shear stress path is a linear relation. In
volumetric deformation induced, closure of micro-cracks may cause of the
disappearance of plastic strain at high level of confining stress and results in a greater
bulk modulus as well under hydrostatic stress. Volumetric deformation induced by
shear stress results shows that the sandstone tends to dilate elastically upon shearing.
The plastic deformation is comprised of a compression at an earlier stage and a
significant dilation at subsequent stages, especially when the shear stress is close to the
shear strength of the sandstone. The total deformation shows a significant dilation
resulting from both the elastic and the plastic behavior. Figure 2.12 shows plastic
deformation vectors obtained from the pure shear and conventional triaxial tests. The
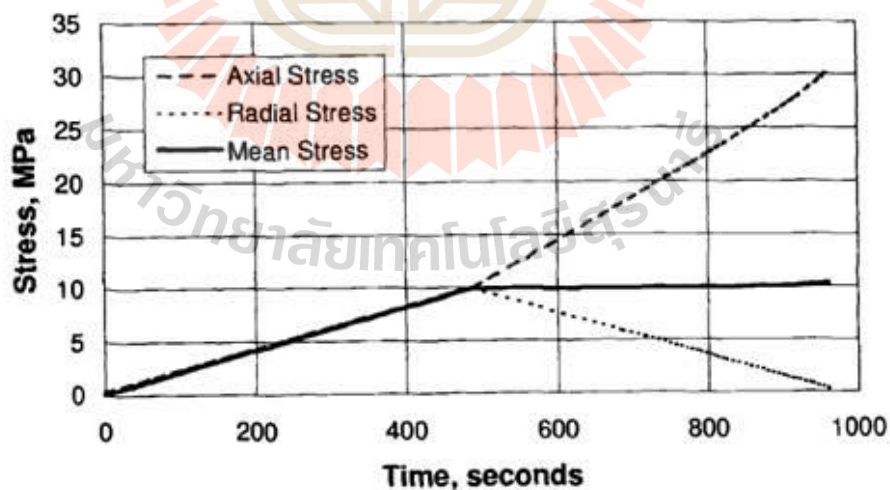
Figure 2.10 Measured load path for typical constant mean stress test (Mellegard and
Pfeifle, 1999).
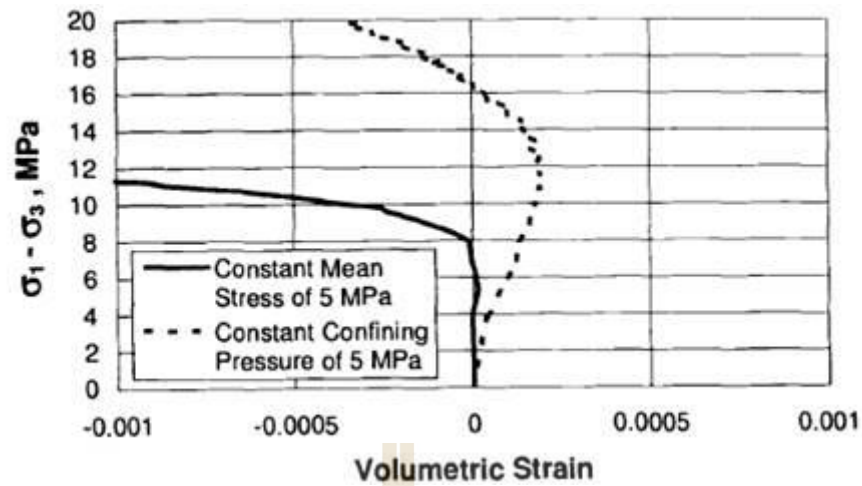
Figure 2.11 Determination of dilation limit by constant mean stress test and constant

confining stress test (Mellegard and Pfeifle 1999).
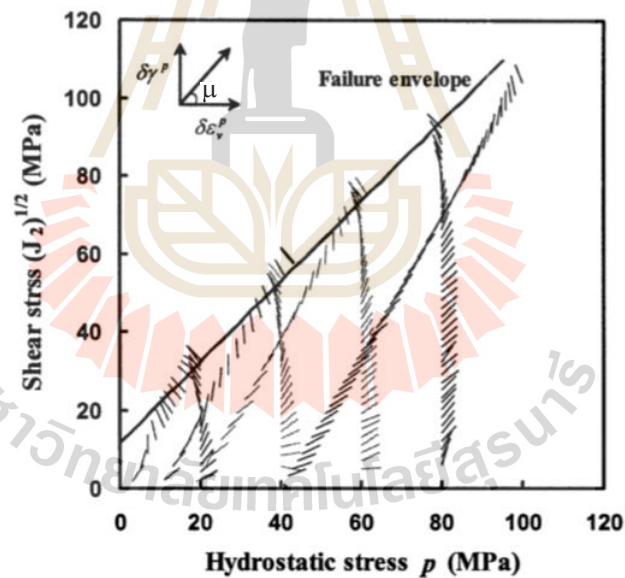
Figure 2.12 Vectors of plastic strain obtained from pure shear and conventional triaxial

compression tests (Modified from Jeng et al., 2002).

plastic deformation vectors (μ) indicate a compression (0 to 90º) or a dilation (greater

than 90º). The final vector tends to be perpendicular to the failure envelope. Those

indicate a typical rule of plastic flow. The result of strength of the conventional triaxial test tends to be higher than that of pure shear test (under approximately hydrostatic stress of 100 MPa).

Weng and Ling (2013) study deformation of Mushan sandstone by performing on three triaxial tests with different hydrostatic pressure. The stress path comprises a constant triaxial compression test (CTC), pure shear test (PS) and reduced triaxial extension tests (RTE), as shown in Figure 2.13. Mushan sandstone is identified to a weak rock and was deposited under sedimentary environment in Micocene. The results show that the volumetric compactions of CTC path are larger than those of PS path because of the increase of hydrostatic stress. The PS path under constant hydrostatic stresses of 40 and 60 MPa exhibits that the deformations are not large in both shear and volumetric strain. The RTE path have much larger volumetric dilation because of the decrease of hydrostatic stress during the tests. The volumetric dilation is more
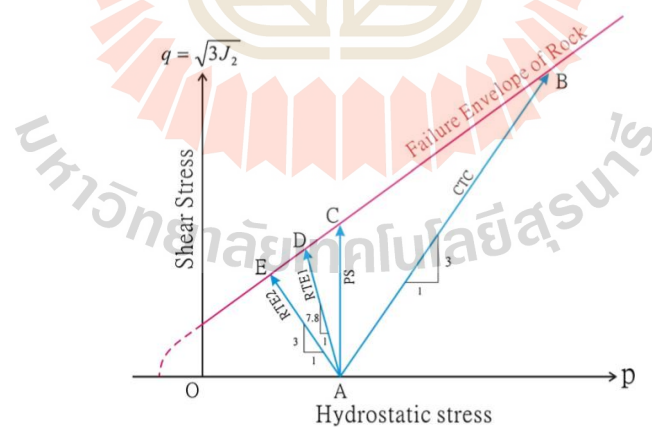
Figure 2.13 Stress paths of hydrostatic compression test, reduced triaxial extension tests, pure shear test and conventional triaxial compression test (Weng and Ling, 2013)

pronounced in RTE2 than RTE1 paths because it has more reduction of hydrostatic stress than RTE1 path does.

Komenthammasopon (2014) studies the effects of stress paths on the strength of PhuPhan and Phu Kradung sandstones by performing to polyaxial compression tests. The specimens are prepared to obtain cubical specimens of nominal dimension of $55 \times 55 \times 55$ mm^3. The different stress paths of the polyaxial compression tests have five paths: (1) σ_1 increases while $\sigma_2 = \sigma_3$ are constant; (2) σ_1 increases while σ_2 and σ_3 decrease (constant σ_m); (3) $\sigma_1 = \sigma_2$ increase while σ_3 is constant; (4) $\sigma_1 = \sigma_2$ increase while σ_3 decreases (constant σ_m); (5) σ_1 increases with varied σ_2 and σ_3 ($\sigma_1 \geq \sigma_2 \geq \sigma_3$). The σ_2 has strong influence on different strengths of specimens under each stress path. The strength of inconstant σ_m path ((1), (3) and (5)) is higher than the constant σ_m ((2) and (4)) because the effect of σ_2 tends to be more pronounced under higher σ_3. The modified Wiebols and Cook criterion and the empirical Mogi criterion can well describe the strengths for all test conditions.

Artkhonghan and Fuenkajorn (2015) study the strength and stiffness of rock salt under different stress paths. The specimens are prepared from the Maha Sarakham formation at depths of 150 to 300 m. The rectangular blocks have a nominal dimension of 44x44x88 cm^3. Four different stress paths are separated to: (1) σ_1 increases while $\sigma_2 = \sigma_3$ are constant (constant σ_3); (2) σ_1 increases while σ_2 and σ_3 simultaneously decrease (constant σ_m); (3) $\sigma_1 = \sigma_2$ increase while σ_3 is constant (constant σ_3); and (4) $\sigma_1 = \sigma_2$ increase while σ_3 decreases (constant σ_m). The elastic modulus and Poisson's ratio tend to be independent of the stress path. Under similar condition, the yield strength of the triaxial compression test with constant σ_3 is higher than those of the triaxial extension test. The yield of stress paths with constant σ_3 is higher than the one with constant σ_m

which results from the influence of σ_2 and σ_3. Testing under constant σ_m is desirable and should provide the results close to the in-situ condition, particularly for the underground structures (tunnels and mine openings). The modified Wiebols and Cook criterion can well predict the triaxial strengths under different stress paths as show in Figure 2.14.

2.5   Conventional shear tests

The shear strength is simulated from the conventional direct shear test (e.g., ASTM D5608-16). The limitation of the direct shear test is that the normal stress on the fracture is limited by the uniaxial compressive strength of the rock. The triaxial shear test is proposed to simulate the friction resistance of core containing an inclined fracture by using pressure cell (e.g., Jaeger et al., 2007).

Byerlee (1967) studies the shearing behavior of Westerly granite under high confining pressures. The specimens are prepared in a cylindrical shape and separated to on three types of fracture surfaces including: ground surface (smooth surface),
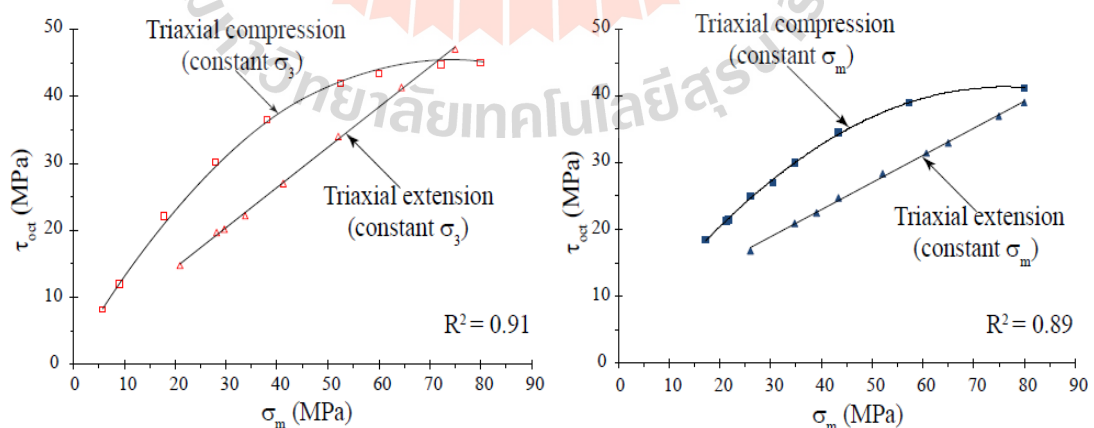
Figure 2.14 Test results fitted by modified Wiebols and Cook criterion (Artkhonghan and Fuenkajorn, 2015).

fracture surface (rough fracture) and virgin rock (intact rock). Comparation between the fracture and the virgin specimens is shown in Figure 2.15, it presents the limitation of brittle-ductile transition in rocks. The two curves of relations intersect at the normal stress of 17.5 kb (confining pressure about of 10 kb). They describe that the stress-stain curve under confining pressure 10 kb is similar a ductile material. That agrees with Orowan (1960) and Maurer (1965) that the apparent ductility of brittle materials may be caused the friction strength (rough fracture) equal to or greater than fracture strength (virgin specimen). Figure 2.16 shows the stress-stain relation and the stick slip motion of the fracture surface developed in virgin rock at failure under high confining pressure.
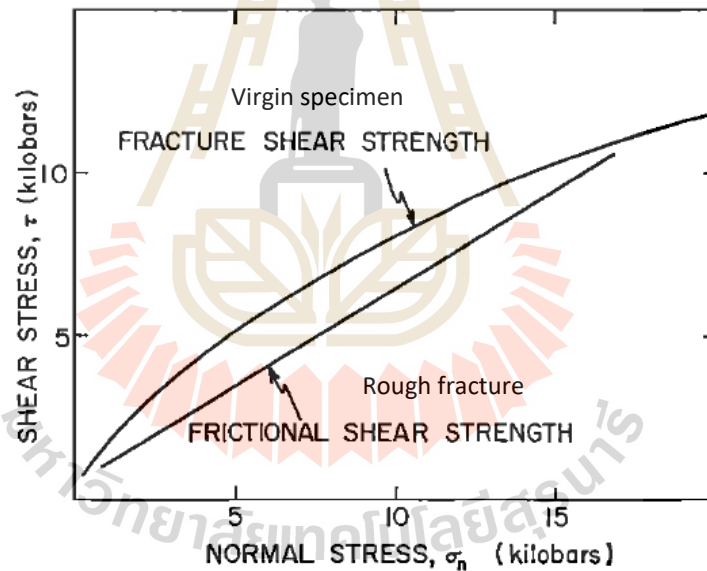
Figure 2.15 Fracture and frictional shear strength versus normal stress for Westerly granite (Modified from Byerlee, 1967).
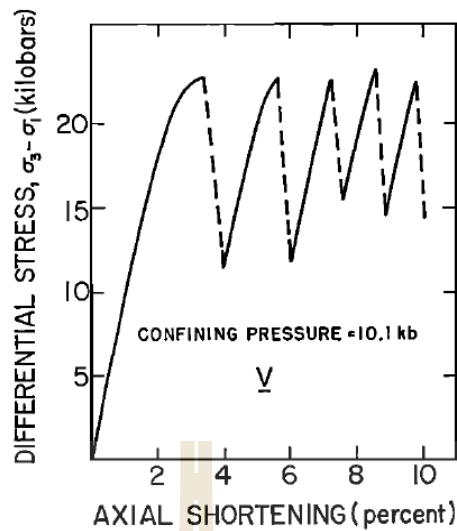
Figure 2.16 Difference stress as a function of axial stain at confining stress of 10.1 kb
for virgin specimens (Byerlee, 1967).

The magnitude of the force is dropped during the process. It can be described the
behavior of fault that released energy in the earthquake.

Barton (1976) develops the empirical shear strength of fracture at low stress.
The direct shear tests are performed on artificial tension fracture. From the results, the
dilation angle is defined as in fact the maximum dilation angle for a given level of
normal stress. The linear relations are proposed as follows:

$$\tau/\sigma_n = \tan(2 \cdot d_n + 30°) \tag{2.1}$$

$$d_n = 10 \cdot \log_{10}(\sigma_c/\sigma_n) \tag{2.2}$$

where σ_c is unconfined compression strength.

Substitute Equation (2.2) to (2.1) obtained as follows:

$$\tau = \sigma_n \cdot \tan(20 \cdot \log_{10}\sigma_c/\sigma_n + 30°) \tag{2.3}$$

The majority of unweathered rock surface has σ_b ranging from 25º to 35º. The roughest end of the spectrum seems to be correctly described in Equation (2.3) by joint roughness coefficient (JRC=20). Joint wall compressive strength (JCS) is equal to the unconfined compression strength of the rock if the joint is unweathered, but may reduce to approximately ($1/4 \cdot \sigma_c$,) if the joint walls are weathered. The JRC varies from 20 (Roughest) to 0 (Smoothest) of spectrum. The equation is generalized from Equation (2.3) as follows:

$$\tau = \sigma_n \cdot \tan(JRC \cdot \log_{10} JCS/\sigma_n + \sigma_b) \tag{2.4}$$

Triaxial shear test results under high confining stresses are fitted with Equation (2.4). There is an increase error between the prediction and the test results. If the normal stress is higher than unconfined compression strength of the rock, the shear strength is over the prediction values. The area of joint contact is increased under high confining pressure that causes increasing the compressive strength of asperities. The JCS in Equation (2.4) is replaced by the difference stress ($\sigma_1 - \sigma_3$). The empirical equation is generalized form Equation (2.4) as follows:

$$\tau = \sigma_n \cdot \tan(JRC \cdot \log_{10}(\sigma_1 - \sigma_3)/\sigma_n + \sigma_b) \tag{2.5}$$

where σ_1 is axial stress and σ_3 is confining stress.

Zhao (1997) states that the JRC-JCS model (Barton's JRC-JCS shear strength criterion 1976) tends to over-predict the shear strength for those natural joints with less matched surfaces. To overcome this shortcoming, a new JRC-JMC shear strength criterion is proposed in order to include the effects of both joint surface roughness and

joint matching, in the form of $\tau = \sigma_n \cdot \tan[JRC \cdot JMC \cdot \log 10(JCS/\sigma_n) + \sigma_b]$. The new JRC-JMC model provides appropriate fining of the shear test results and gives a better interpretation and prediction, particularly for natural joints that do not have perfectly matched surfaces.

Ramamurthy and Arora (1994) test jointed rock under unconfined and confined stress of three materials, namely, Plaster of Paris, Jamrani sandstone and Agra sandstone. Plaster of Paris represent soft rock that is flexibility and quick hardening. Jamrani sandstone is form the Jamrani Hydel Project, Uttar Pradesh. The size is same Plaster of paris. Agra sandstone is obtained from Agra, Uttar Pradesh consisting primarily of quartz. All of materials is prepared in axisymmetric size of 38 mm in diameter and 76 mm in height. The jointed rock inclination varies from 0-90°. The lowest unconfined compressive strength occurs at angle ranging from 30-40° that closed to the theoretically derived value of $(45 - \phi/2)$ for frictional materials. The axial stress is the most probable sliding joint. The effect of the induced anisotropy reduces when the confining stresses increase over 2.5 MPa as shows in Figure 2.17.

Kleepmek et al. (2016) study the effects of displacement velocity on frictional behavior of fractures rock. The triaxial shear testing is performed on Tak granite, Phra Wihan sandstone and Lopburi marl by using a polyaxial load frame. All test is controlled displacement velocity ranging from 1.15×10^{-5} to 1.15×10^{-2} mm/s. The specimens are prepared to obtain regular blocks with the nominal dimensions of $50 \times 50 \times 87$ mm^3. The fractures are artificially made in tension-induced fracture and saw-cut surface that normal to the fracture plane made angle of 59.1° with the specimen vertical axis. They have shear area of 50×100 mm^2. The confining pressure of the tension-induced fractures are maintained constant at 1, 3, 7, 12 and 18 MPa and 1, 7

and 12 MPa for saw-cut surfaces. Neoprene sheets cover the specimen to minimize the friction between loading platen and specimen before installing in the frame. The specimen is first under hydrostatic load. The testing is stopped when the total vertical displacement of 5 mm is reached. The peak stresses are occurred within 2 mm and the residual stresses are constant up to 5 mm of shear displacement.

They proposed the calculation of shear (d_s) and normal (d_n) displacement from vertical (d_1) and lateral (d_3) displacement as follows:

$$d_s = d_1/\sin\beta \qquad (2.8)$$
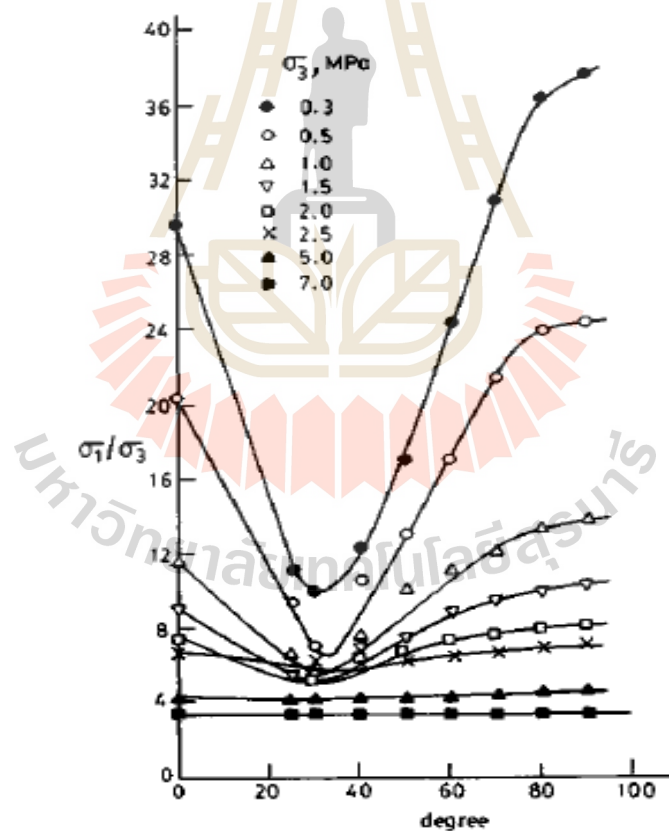
Figure 2.17 Variation of σ_1/σ_3 as a function of inclination of single joint for Plaster of Paris (Modified from Ramamurthy and Arora, 1994).

$$d_n = (d_{3,m} - d_{3,c})\sin\beta \qquad\qquad (2.9)$$

$$d_{3,c} = \tan(90-\beta)d_1 \qquad\qquad (2.10)$$

where $d_{3,m}$ is the total lateral displacement measured during the test, $d_{3,c}$ is the calculated lateral displacement induced by the vertical displacement on the incline fracture plane and β is the angle between axial stress and normal stress axes.

The shear strengths and residual stresses reduce with increasing velocity. The shear velocity more affects to higher JRC (Tak granite) than lower JRC (Phra Wihan sandstone and Lopburi marl). On the saw-cut surfaces, the shear strength is independent on velocity of sliding. Proposed criterion gives a reasonably good transition from the high confinement shear strengths to the unconfined condition test (direct shear test).

The anisotropic stresses have been performed on the fractures to determine the peak shear strengths by Kapang et al. (2013). The specimens are prepared from the Phu Kradung (PKSS), Phu Phan (PPSS) and Phra Wihan (PWSS) sandstones. They are cut to obtain rectangular blocks with nominal dimensions of $76\times76\times126$ mm^3. The angle between normal stress to the inclined fracture and the axial stress is 59.1º. It is found that the stress parallel to the fracture can decrease the fracture shear strengths.

2.6   Strain energy density

Beer et al. (2012) state that the strain energy is defined as the increase in energy associated with the deformation and equal to the work done by applying the load to materials. The strain energy density at a given point is divided into two parts. Mean strain energy density is a change in volume of the materials at that point. Distortional strain energy density is a distortion, or change in shape of the material at the same point:

Sriapai et al. (2012) propose the strain energy density criterion to describe the salt strength and deformability under different temperatures. It is assumed that under a given mean strain energy and temperature the distortional strain energy required to fail the salt specimens is constant. Regression on the test results shows that the distortional strain energy increases linearly with the mean strain energy. It is interesting to note that the rates of the increase of the distortional strain energy with respect to the mean strain energy are virtually the same for all temperature levels.

Fuenkajorn et al. (2012) propose empirical strength criteria based on the strain energy density principle of rock salt by performing the uniaxial and triaxial compression tests to assess the influence of loading rate on the compressive strength and deformability of the Maha Sarakham salt. The salt specimens with a nominal dimension of $5.4 \times 5.4 \times 5.4$ cm^3 are compressed to failure using a polyaxial load frame. The lateral confining pressures are maintained constant at 0, 3, 7, 12, 20 and 28 MPa while the axial stresses are increased at constant rates of 0.001, 0.01, 0.1, 1.0 and 10 MPa/s until failure occurs. The salt elasticity and strength increase with the loading rates. The elastic (tangent) modulus determined at about 40% of the failure stress varies from 15 to 25 GPa, and the Poisson's ratio from 0.23 to 0.43. The elastic parameters tend to be independent of the confining pressures. The strains induced at failure decrease as the loading rate increases. Various multiaxial formulations of loading rate dependent strength and deformability are derived. The variation of the octahedral shear stresses and strains induced at dilation and at failure with the applied shear stress rates can be best described by power relations. The distortional strain energy at dilation and at failure from various loading rates varies linearly with the mean normal stress. The proposed empirical criteria are applied to determine the safe maximum withdrawal rate

of a compressed-air energy storage cavern in the Maha Sarakham salt formation. The strain energy criterion that considers both distortional and mean stress–strains at dilation tends to give the most conservative results.

Sartkaew and Fuenkajorn (2013) perform the uniaxial compression test to evaluate the effects of loading rate on compressive strength and deformability of the Maha Sarakham salt under temperatures ranging from 273 to 373 Kelvin. The variation of the octahedral shear strength with the stress rates and temperatures can be described by logarithmic relations. The distortion strain energy criterion is proposed to describe the salt strength under varied stress rates and temperatures. The criterion can be used to determine the stability of salt around compressed-air energy storage caverns, where the loading rates and temperatures are continuously varied during air injection and retrieval periods.

Khamrat et al. (2018) perform triaxial shear tests on tension-induced fractures and smooth saw-cut surfaces in Tak granite under temperatures up to 773K. The objective of this work is to gain an understanding of the movement of shallow faults that cause seismic activities in the Tak batholith in the north of Thailand. The strain energy principle is applied to incorporate the principal stresses and strains into a strength criterion. A linear relation between the distortional strain energy and the mean strain energy of the fractures is obtained. The W_d-W_m slope depends on the fracture roughness and strength of the asperities, which can be defined as a function of shear and mean strains and dilation of the fractures. This may allow predicting the strength of the shallow faults in the Tak batholith by calculating the changes of the energy ratios from the displacements monitored along the fault line.

CHAPTER III

SAMPLE PREPARATION

3.1 Introduction

This chapter describes the sample preparation and specifications for the triaxial and direct shear tests on rough (tension-induced) and smooth (saw-cut) fractures. Asperity amplitudes on fractures are identified to determine the joint roughness coefficient of the rough fracture specimens.

3.2 Sample preparation

Rock specimens are prepared from Phra Wihan sandstone. These specimens are classified as fine-grained quartz with highly uniform texture and density. Related study performed by Khamrat et al. (2016) and Kleepmek et al. (2016) have determined the mineral compositions and mechanical properties of the sandstone obtained from the same source location. It comprises 72% quartz (0.2-0.8 mm), 20% feldspar (0.1-0.8 mm), 3% Mica (0.1-0.3 mm), 3% rock fragment (0.5-2 mm) and 2% other (0.5-1 mm). The average density is 2.21±0.25 g/cc. The uniaxial compressive strength is 48±11 MPa, cohesion is 10 MPa and friction angle is 46º. Based on the classification by International Society for Rock Mechanics (Hoek and Brown, 1997) the sandstone is classified as medium strong rock.

A line load is applied to obtain a tension-induced fracture diagonally across the block specimen, as shown in Figure 3.1. The specimens are then cut to obtain regular

blocks with nominal dimension of $50 \times 50 \times 87$ mm^3. The smooth fractures are artificially made by using a universal masonry saw (Husqvarna TS400F). They are also cut along the diagonal line of the specimen. The prepared fractures have nominal areas of 50×100 mm^2. The normal to the fracture plane makes an angle (β) of 60° with the main axis of the specimen, as shown in Figure 3.2.

The specimens for direct shear testing are prepared to have nominal dimensions of $100 \times 100 \times 160$ mm^3 (Figure 3.3). The tension-induced and saw-cut fractures are made at the mid-section of the specimens. The nominal fracture area is 100×100 mm^2. All fractures are clean and well mated. Figure 3.4 shows some laser scanned images of rough fractures. All laser scanned images of rough surfaces are shown in Appendix A. For the specimens with the smooth fracture, two specimen blocks of rock are used to form a complete pair of specimens primarily to avoid the effect of the groove caused by the cutting blade. Figure 3.5 shows some smooth fracture specimens for triaxial shear tests.

The asperity amplitudes for the rough (tension-induced) fractures are measured from the laser-scanned profiles along the shear direction. The fracture profile readings are made to the nearest 0.001 mm. The maximum amplitudes are used to determine the joint roughness coefficients (JRC) of each fracture by using Barton's chart (Barton, 1982). The example of determined JRC value is shown in Appendix B. The JRC values averaged from all rough fractures are 8. Tables 3.1 to 3.6 show physical properties of rough and smooth fractures. Tables 3.7 to 3.10 show fracture profiles of rough fractures.
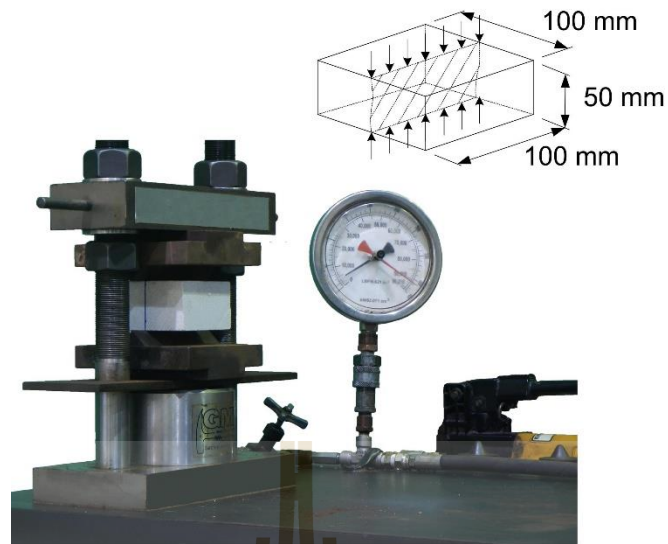
Figure 3.1 Line load method.

Figure 3.2 Some rough fracture specimens prepared for triaxial shear test.
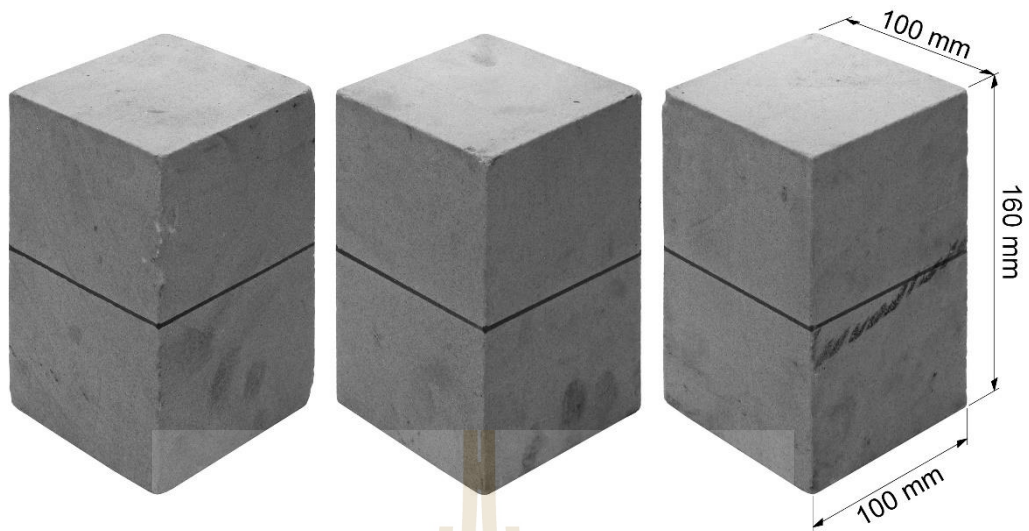
Figure 3.3 Some rough fracture specimens prepared for direct shear test.
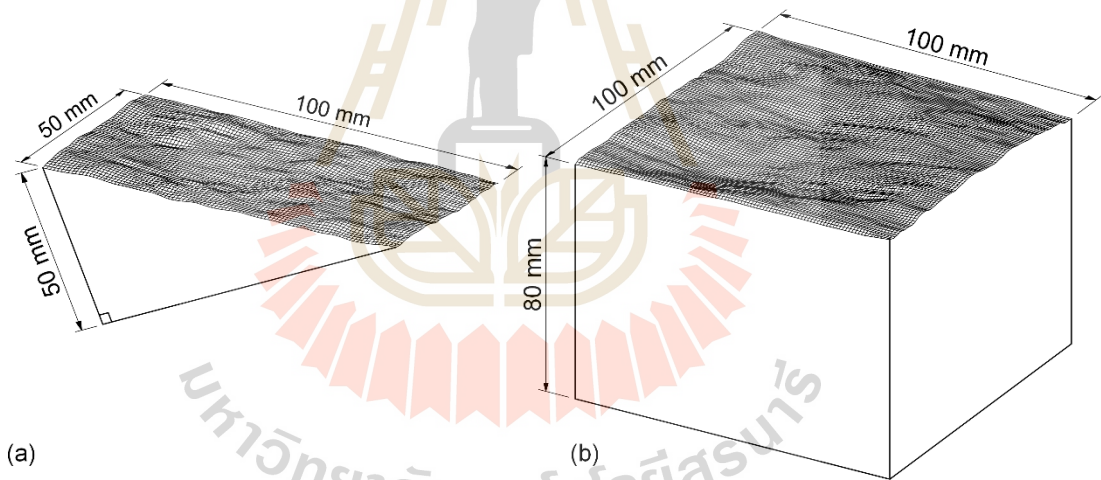
Figure 3.4 Laser scanned images of rough fractures for triaxial shear test (a) and direct shear test (b).
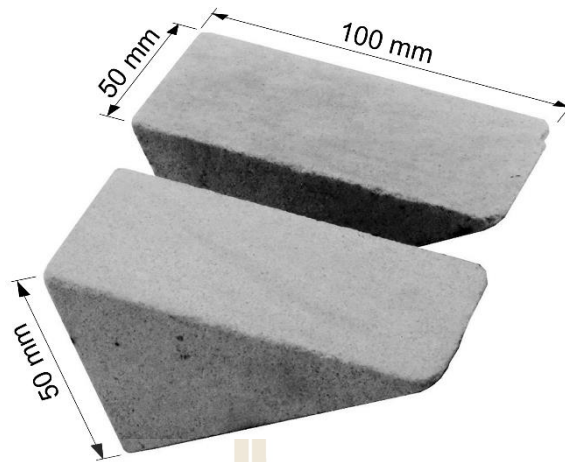
Figure 3.5 Smooth fracture specimens prepared for triaxial shear test.

Table 3.1 Summary of rough fracture dimensions under constant mean stress.

Specimen No.	Average Width (mm)	Average Length (mm)	Average Height (mm)	Weight (g)	Density (g/cc)
CMS-PWS-TI-1	51.13	55.92	84.34	559.45	2.32
CMS-PWS-TI-2	54.92	53.28	86.68	596.04	2.35
CMS-PWS-TI-3	54.73	50.83	89.11	567.68	2.29
CMS-PWS-TI-4	54.43	54.43	89.89	620.50	2.33
CMS-PWS-TI-5	54.22	53.52	88.12	598.36	2.34
CMS-PWS-TI-6	55.68	54.52	85.50	607.34	2.34
CMS-PWS-TI-7	54.72	53.16	87.46	574.97	2.26
CMS-PWS-TI-8	54.44	52.28	89.30	584.56	2.30

Table 3.2 Summary of rough fracture dimensions under constant confining stress.

Specimen No.	Average Width (mm)	Average Length (mm)	Average Height (mm)	Weight (g)	Density (g/cc)
CCS-PWS-TI-1	52.53	53.53	88.82	576.93	2.31
CCS-PWS-TI-2	51.36	54.34	88.90	565.69	2.28
CCS-PWS-TI-3	50.46	54.27	87.44	536.37	2.24
CCS-PWS-TI-4	49.88	52.77	86.02	520.76	2.30
CCS-PWS-TI-5	51.31	54.10	86.93	550.17	2.28

Table 3.3 Summary of rough fracture dimensions under constant normal stress.

Specimen No.	Average Width (mm)	Average Length (mm)	Average Height (mm)	Weight (g)	Density (g/cc)
CNS-PWS-TI-1	102.11	103.12	158.22	3865.09	2.32
CNS-PWS-TI-2	98.95	100.24	161.10	3547.36	2.22
CNS-PWS-TI-3	101.32	99.70	159.88	3617.69	2.24
CNS-PWS-TI-4	103.56	101.70	160.46	3819.33	2.26

Table 3.4 Summary of rough fracture dimensions under constant shear stress.

Specimen No.	Average Width (mm)	Average Length (mm)	Average Height (mm)	Weight (g)	Density (g/cc)
CSS-PWS-TI-1	98.90	100.30	158.93	3499.90	2.22
CSS-PWS-TI-2	102.14	100.43	160.56	3886.94	2.36
CSS-PWS-TI-3	99.68	99.76	158.20	3649.71	2.32
CSS-PWS-TI-4	103.20	100.86	162.14	3814.14	2.26

Table 3.5 Summary of smooth fracture dimensions under constant mean stress.

Specimen No.	Average Width (mm)	Average Length (mm)	Average Height (mm)	Weight (g)	Density (g/cc)
CMS-PWS-SC-1	50.50	53.00	90.00	554.03	2.30
CMS-PWS-SC-2	51.20	51.00	87.40	529.46	2.32
CMS-PWS-SC-3	51.00	52.00	89.00	542.86	2.30
CMS-PWS-SC-4	48.50	55.00	87.50	560.17	2.40
CMS-PWS-SC-5	48.00	52.00	89.00	510.93	2.30
CMS-PWS-SC-6	53.00	51.00	90.00	554.65	2.28
CMS-PWS-SC-7	51.50	50.00	86.00	509.33	2.30
CMS-PWS-SC-8	54.90	51.60	87.40	569.45	2.30

Table 3.6 Summary of smooth fracture dimensions under constant confining stress.

Specimen No.	Average Width (mm)	Average Length (mm)	Average Height (mm)	Weight (g)	Density (g/cc)
CCS-PWS-SC-1	51.80	53.60	89.00	568.34	2.30
CCS-PWS-SC-2	52.50	52.00	89.80	558.95	2.28
CCS-PWS-SC-3	53.00	51.00	89.50	551.57	2.28
CCS-PWS-SC-4	54.50	52.00	89.00	582.64	2.31
CCS-PWS-SC-5	53.00	54.50	89.00	598.98	2.33

Table 3.7 Summary of rough fracture profiles under constant mean stress.

Specimen No.	Fracture profiles	JRC
CMS-PWS-TI-1	Amplitude of asperity = 1.95 mm	8
CMS-PWS-TI-2	Amplitude of asperity = 1.86 mm	7
CMS-PWS-TI-3	Amplitude of asperity = 2.00 mm	8
CMS-PWS-TI-4	Amplitude of asperity = 1.61 mm	7
CMS-PWS-TI-5	Amplitude of asperity = 1.89 mm	8
CMS-PWS-TI-6	Amplitude of asperity = 1.90 mm	8
CMS-PWS-TI-7	Amplitude of asperity = 2.04 mm	8
CMS-PWS-TI-8	Amplitude of asperity = 1.46 mm	6
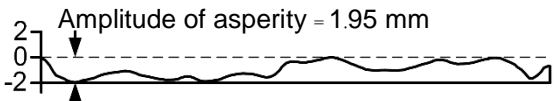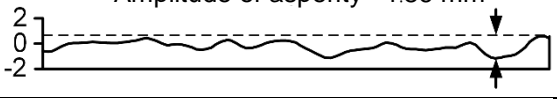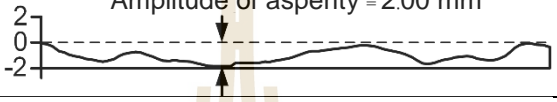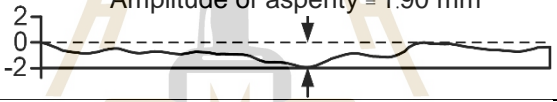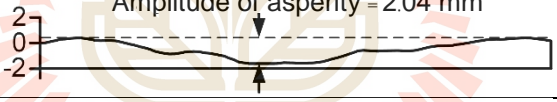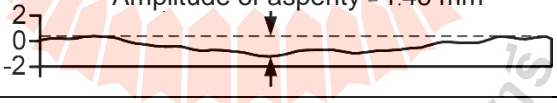
Table 3.8 Summary of rough fracture profiles under constant confining stress.

Specimen No.	Fracture profiles	JRC
CCS-PWS-TI-1	Amplitude of asperity = 1.82 mm	7
CCS-PWS-TI-2	Amplitude of asperity = 1.99 mm	8
CCS-PWS-TI-3	Amplitude of asperity = 2.11 mm	8
CCS-PWS-TI-4	Amplitude of asperity = 1.72 mm	7
CCS-PWS-TI-5	Amplitude of asperity = 2.05 mm	8
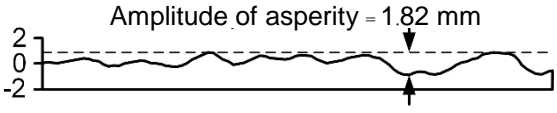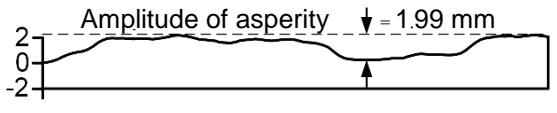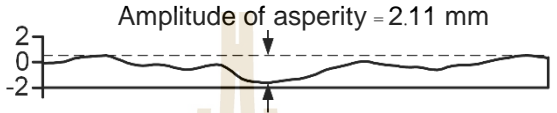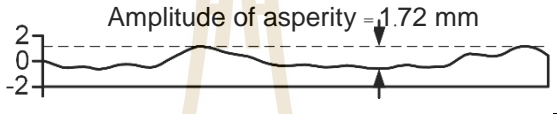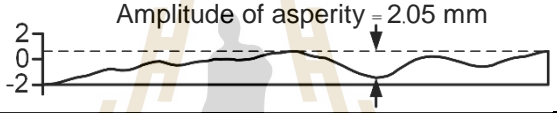
Table 3.9 Summary of rough fracture profiles under constant normal stress.

Specimen No.	Fracture profiles	JRC
CNS-PWS-TI-1	Amplitude of asperity = 2.00 mm	8
CNS-PWS-TI-2	Amplitude of asperity = 1.96 mm	8
CNS-PWS-TI-3	Amplitude of asperity = 2.07 mm	8
CNS-PWS-TI-4	Amplitude of asperity = 2.03 mm	8
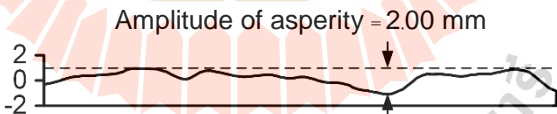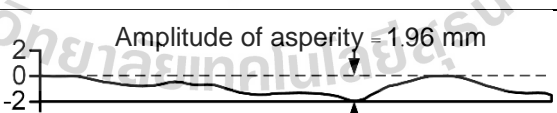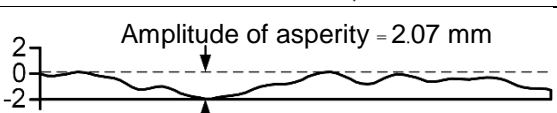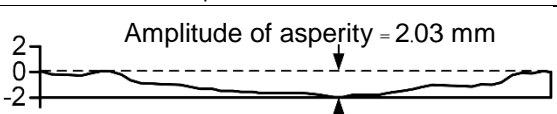
Table 3.10 Summary of rough fracture profiles under constant shear stress.

Specimen No.	Fracture profiles	JRC
CSS-PWS-TI-1	Amplitude of asperity = 1.88 mm	8
CSS-PWS-TI-2	Amplitude of asperity = 1.94 mm	8
CSS-PWS-TI-3	Amplitude of asperity = 1.94 mm	8
CSS-PWS-TI-4	Amplitude of asperity = 1.78 mm	7
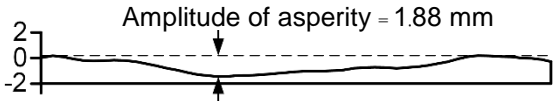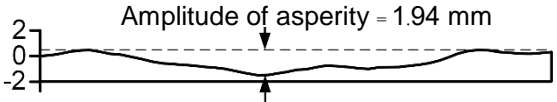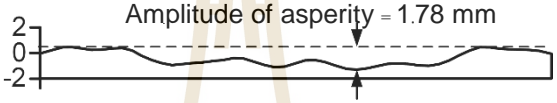
CHAPTER IV

LABORATORY TESTING

4.1   Introduction

The laboratory work includes the triaxial shear and the direct shear tests. This chapter describes the apparatus, methods and calculations of shear strength and deformation of fracture specimen.

4.2   Triaxial shear test

4.2.1   Test apparatus

The triaxial shear tests are performed by using the true triaxial load frame (Komenthammasopon, 2014) (Figure 4.1). The frame comprises four main components: three mutually perpendicular load frames, six 100-ton hydraulic cylinders, measurement system and three hydraulic pumps. Each load frame has two supporting steel plates, which are connected by 4 steel rods. The spacing between two steel plates about 610 mm. The steel plates have dimension of $430{\times}430{\times}38$ mm^3 and other two (in vertical axes) are $300{\times}300{\times}60$ mm^3. During the test each set of the three load frames applies independent loads to provide different principal stresses on to the rock specimens. The measurement system includes include three 4-inch pressure gages and four displacement dial gages. The three pressure gages are installed at three hand pumps to measure the applied load, while the four dial gages measure the deformation along the three principal axes for further stain calculation (two dial gages are used to

monitor the vertical axes). This loading device can accommodate the cubic or rectangular specimens of different sizes by adjusting the distances between the opposite steel platens. For this work, the rock specimens have the nominal dimensions of $50{\times}50{\times}87$ mm^3, placed around the center of the device. One of the lateral (horizontal) stresses is parallel to the strike of the fracture plane and is designated as σ_p. The other is normal to the fracture strike and is designated as σ_o. The testing system is calibrated before testing by using an electronic load cell.
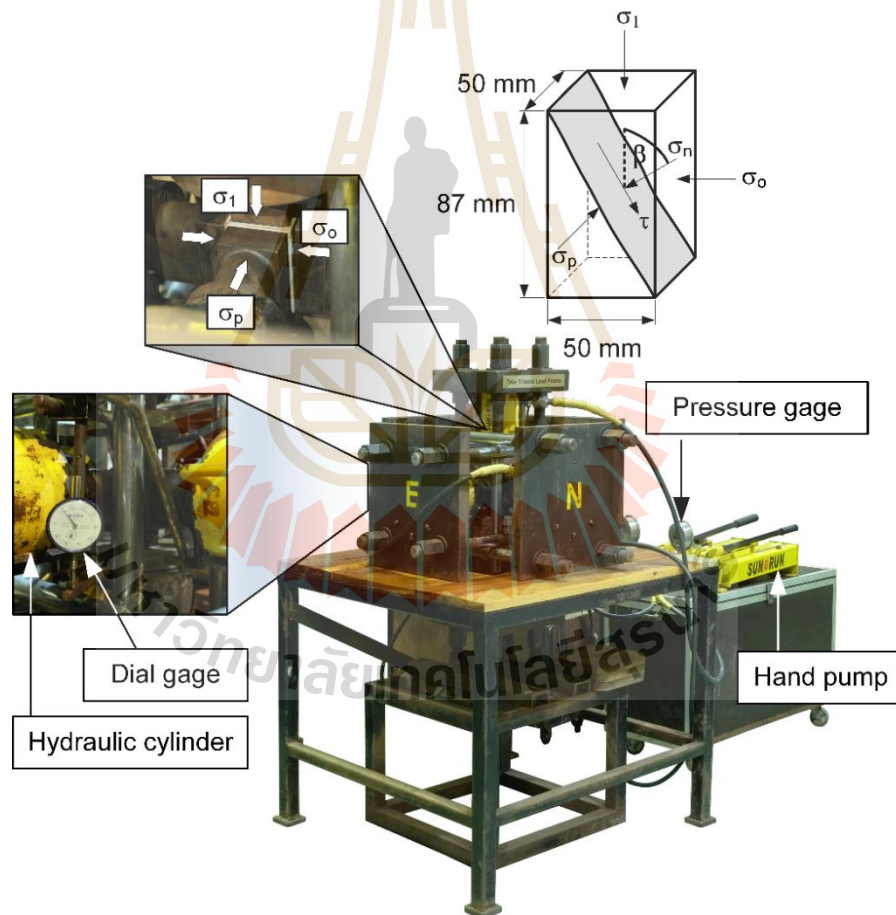
Figure 4.1 True triaxial load frame used to apply three principal stresses, to triaxial shear test specimen.

4.2.2 Test method

The specimens are first covered with neoprene sheet for all sides to minimize the friction between the specimen surfaces and steel plates. The constant σ_o path, which is similar to the conventional triaxial shear test, is conducted by varying the lateral stresses from 1, 3, 7, 12 to 18 MPa. The axial (σ_1) and lateral stresses ($\sigma_p=\sigma_o$) are simultaneously increased to the predefined magnitude of σ_o on the specimen where the τ on the fracture plane is zero. The σ_1 is then increased at the rate of 0.1 MPa/s while the lateral stresses are maintained constant until peak shear strength is reached (Table 4.1a). The test is terminated when the axial displacement of 5 mm is obtained.

The constant σ_m path uses the mean stress $[(\sigma_1+\sigma_o+\sigma_p) / 3]$ ranging from 20, 25, 30, 35, 40, 45, 50 to 55 MPa. The σ_1 and lateral stresses (σ_o and σ_p) are first simultaneously increased to the predefined magnitude of σ_m where the τ on the fracture plane is zero. The σ_1 is then increased at the rate of 0.1 MPa/s while σ_o is decreased under the same rate. The σ_p is maintained constant during the test (Table 4.1b). The test is terminated after the peak shear strength is reached. The specimen deformations are monitored along the three principal loading directions. They are used to calculate the principal strains during loading. The readings are recorded every 1.5 MPa (equivalent to the 50 psi on the pump pressure gages).

The τ and its corresponding σ_n for triaxial shear test can be determined as follows (Jaeger et al., 2007):

$$\tau = 1/2(\sigma_1 - \sigma_o)\cdot\sin2\beta \tag{4.1}$$

$$\sigma_n = 1/2(\sigma_1 + \sigma_o) + 1/2(\sigma_1 - \sigma_o)\cdot\cos2\beta \tag{4.2}$$

where β is the angle between σ_1 and σ_n directions. For all specimens the angle β equals to 60°. The shear and normal displacements (d_s and d_n) can also be determined from the axial and lateral displacements (d_1 and d_o) as follows (Kleepmek et al., 2016):

$$d_s = d_1 \sin\beta \tag{4.3}$$

$$d_n = (d_{o,m} - d_{o,c})\sin\beta \tag{4.4}$$

$$d_{o,c} = \tan(90-\beta)d_1 \tag{4.5}$$

where $d_{o,m}$ is the total lateral displacement measured during the test, and $d_{o,c}$ are the calculated lateral displacement induced by the axial displacement on the smooth inclined fracture plane. The actual lateral fracture dilation along the σ_o axis can be determined by subtracting the measured dilation ($d_{o,m}$) by the calculated dilation caused by the inclined fracture plane, as shown in Equation (4.5).

4.3 Direct shear test

4.3.1 Test apparatus

Direct shear tests are performed under each condition by using a direct shear device (SBEL DR44, capacity of 10,000 pounds normal load and 30,000 pounds shear force) (Figure 4.2). The test method and calculation follow as much as practical the ASTM (D5607-16) standard. Dial gages are used to measure the shear displacement and fracture dilation. The maximum normal stress for the direct shear device is 4 MPa (for 100×100 mm^2 fracture area).

Table 4.1 Stress paths of triaxial shear tests under constant confining stress (a) and constant mean stress (b).

Stress path

(a) Constant σ_o (b) Constant σ_m

σ_o = 1-18 MPa σ_m = 20-55 MPa
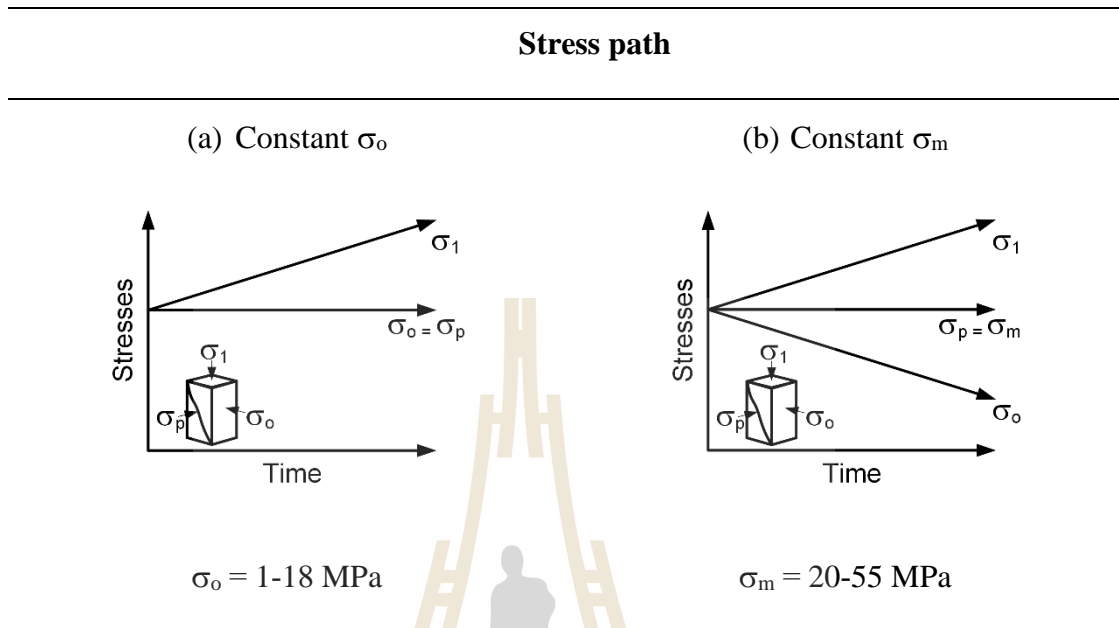
4.3.2   Test method

The constant σ_n path is performed by varying the normal stresses from 1, 2, 3 to 4 MPa. A shear direction is defined. The normal stress is first applied to the predefined magnitude and then maintained constant during the test. The shear stress is increased at the rate of 0.1 MPa/s until a total shear displacement of 5 mm is reached (Table 4.2a).

For constant τ path the normal and shear stress are simultaneously increased to the predefine magnitude, where before shearing $\sigma_n = \tau$, which ranging between 1, 2, 3 and 4 MPa. The shear stress is maintained constant while σ_n is constantly reduced at the rate of 0.1 MPa/s. The test is terminated when dropping of the shear stress is detected (Table 4.2b). The fracture dilation and shear displacements are monitored using high precision displacement gages.

The shear strength is calculated by;

$$\tau = S/A \tag{4.6}$$

where S is shear force and A is contact area between both specimens. Assuming here that the total displacement is small (less than 10 mm), the contact area is taken as constant during the shear tests.
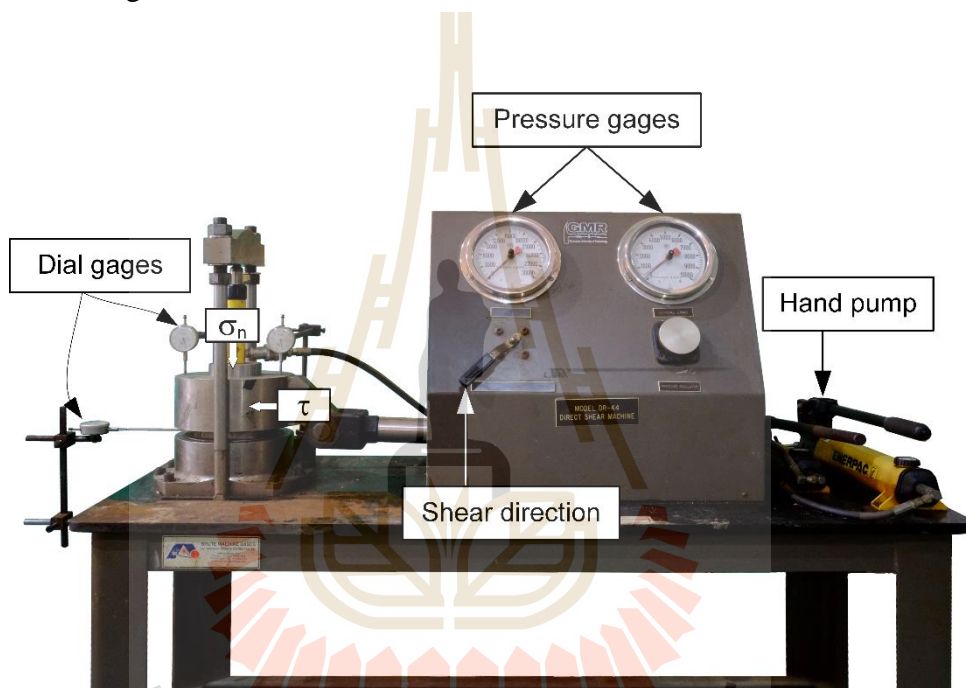
Figure 4.2 Direct shear device (SBEL DR44).

Table 4.2 Stress paths of direct shear tests under constant normal stress (a) and constant shear stress (b).

Stress path

(a) Constant σ_n (b) Constant τ

$\sigma_n = 1\text{-}4$ MPa $\tau = 1\text{-}4$ MPa
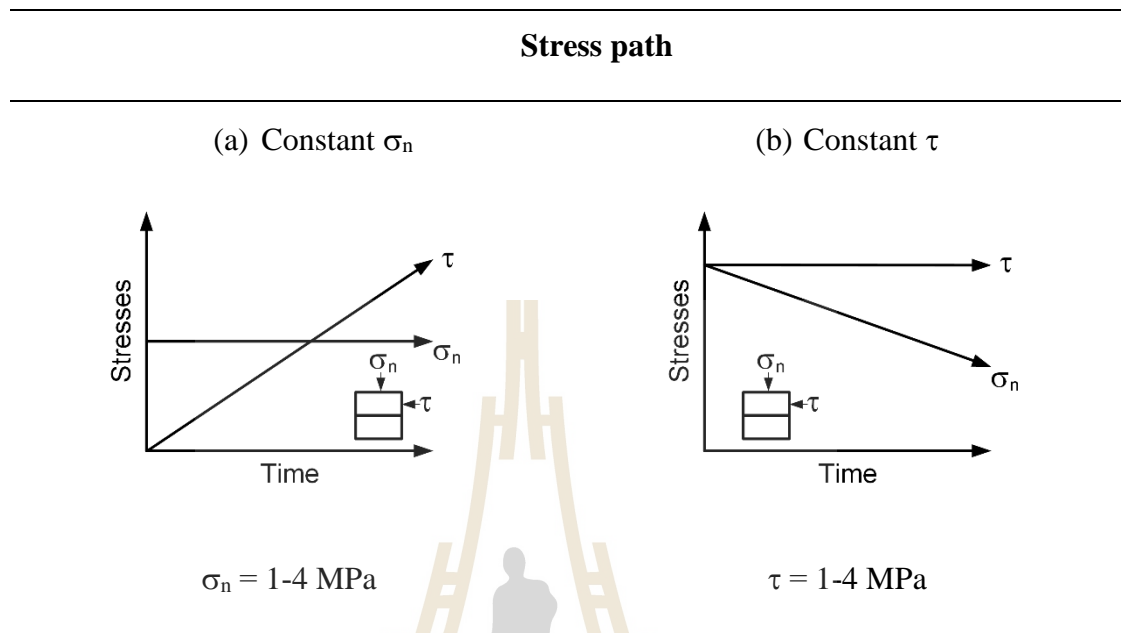
CHAPTER V

TEST RESULTS

5.1 Introduction

This section presents the results of triaxial shear tests on rough and smooth fractures and of direct shear tests on rough fractures. The results are used to develop shear strength criteria. Fracture dilation and post-test observations of rough fracture are also made.

5.2 Triaxial shear tests on rough fractures

The triaxial shear tests are performed under constant σ_o path with σ_o varying from 1, 3, 7, 12 to 18 MPa and under constant σ_m paths with σ_m varying from 20, 25, 30, 35, 40, 45, 50 to 55 MPa. The results are presented in forms of shear stresses-displacements (τ-d_s) curves and shear strengths-normal stresses (τ-σ_n) curves.

5.2.1 Shear stresses-displacements curves

The major principal stresses (σ_1) obtained from both shear stress paths are presented as a function of the vertical displacements (d_1), as shown in Figure 5.1. Shear stresses-displacement (τ-d_s) curves for all tests are shown in Figure 5.2. The shear stresses and displacements are calculated from σ_1 and d_1 by using Equations (4.1) and (4.3) in chapter IV. It is clear that the shear stresses increase with σ_o and σ_m. The peak shear stresses are reached within 1 mm.
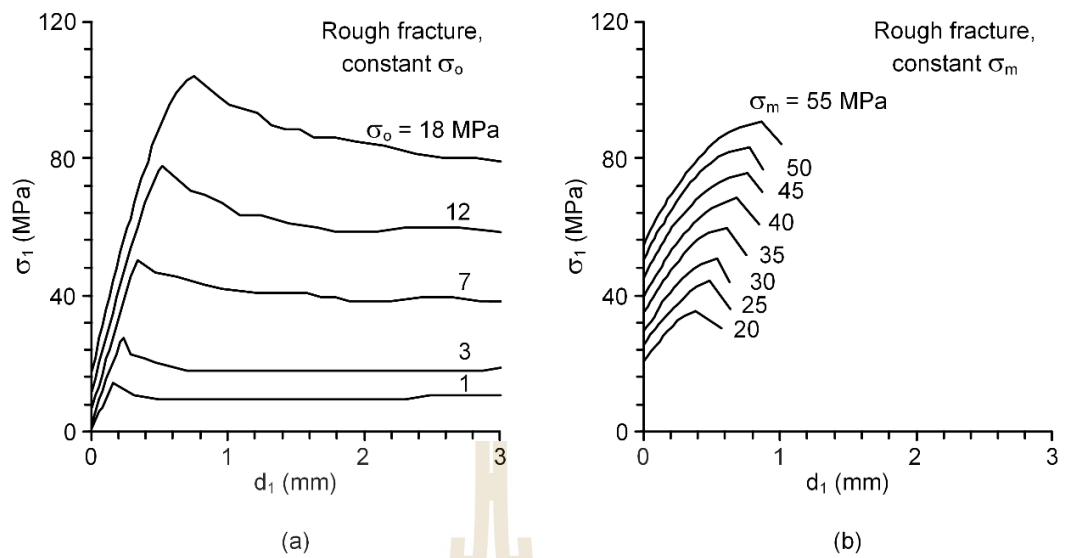
Figure 5.1 Major principal stresses (σ_1) as a function of vertical displacements (d_1) for triaxial shear tests on rough fractures under constant confining stress (a) and constant mean stress (b).
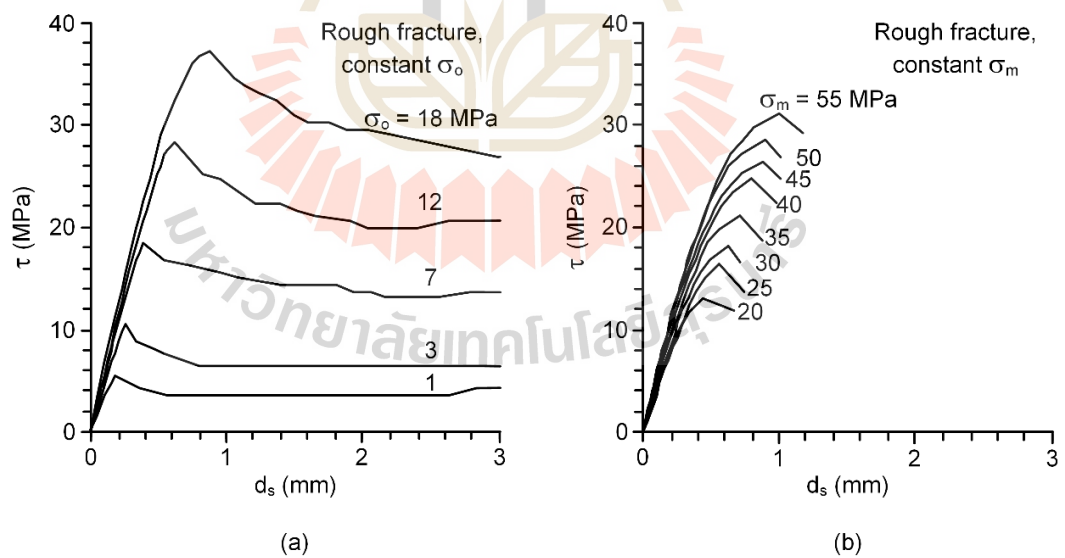
Figure 5.2 Shear stresses (τ) as a function of shear displacements (d_s) for triaxial shear tests on rough fractures under constant confining stress (a) and constant mean stress (b).

For constant σ_o testing the differences between the peak and residual shear stresses notably reduce when the rough fractures are subjected to lower confinements. The residual stresses tend to remain constant within 3 mm. The relations between shear stress and displacement under constant σ_m testing tend to be more non-linearly than those of constant σ_o testing.

For constant σ_m testing the residual shear stress can not be obtained as the σ_m values can not be maintained constant after the peak stress has been reached. Note also that the range of σ_m values used for constant σ_m testing is relatively high compared to the σ_o values used in the constant σ_o testing. This is primarily because when σ_m is lower than 20 MPa the reducing σ_o reaches zero before the peak shear stress is reached.

5.2.2   Shear strengths-normal stresses curves

The results of the triaxial shear tests performed here can be presented in the form of the peak shear stresses-normal stresses diagram. The stresses can be calculated from the σ_1 and σ_o by using Equations (4.1) and (4.2) in the previous chapter. Table 5.1 shows the calculation results for the both stress paths. Figure 5.3 shows the peak shear stresses as a function of normal stresses for both stress paths. The linear relation of the τ-σ_n lines is observed.

The Coulomb criterion is applied to describe the fracture shear strengths obtained from both stress paths:

$$\tau = \sigma_n \tan\phi + c \qquad\qquad (5.1)$$

where ϕ and c are friction angle and apparent cohesion. The criterion fits well to all strength results, as suggested by their good correlation ($R^2 > 0.9$). The friction angle for constant σ_o and constant σ_m paths are determined as 42.0º and 37.4º and the cohesion are 2.25 and 3.52 MPa, respectively. The shear strengths obtained from constant σ_o path tend to be greater than those from constant σ_m path, particularly under high confinements (high σ_o and σ_m values). Under low confinements both stress paths yield similar shear strengths.

Table 5.1 Summary of peak strengths and their corresponding normal stresses for rough fractures.

Paths	σ_o (MPa)	$\sigma_{1,p}$ (MPa)	σ_n (MPa)	τ_p (MPa)
Constant σ_o	1	13.87	4.22	5.57
	3	27.52	9.13	10.62
	7	49.66	17.66	18.47
	12	77.32	28.33	28.28
	18	104.56	39.64	37.48
Constant σ_m	5.22	35.48	12.78	13.10
	7.59	42.72	16.38	15.21
	8.87	50.72	19.33	18.13
	10.59	59.49	22.82	21.17
	11.12	68.40	25.44	24.81
	14.49	75.60	29.77	26.46
	17.28	83.29	33.78	28.58
	18.74	90.66	36.72	31.14
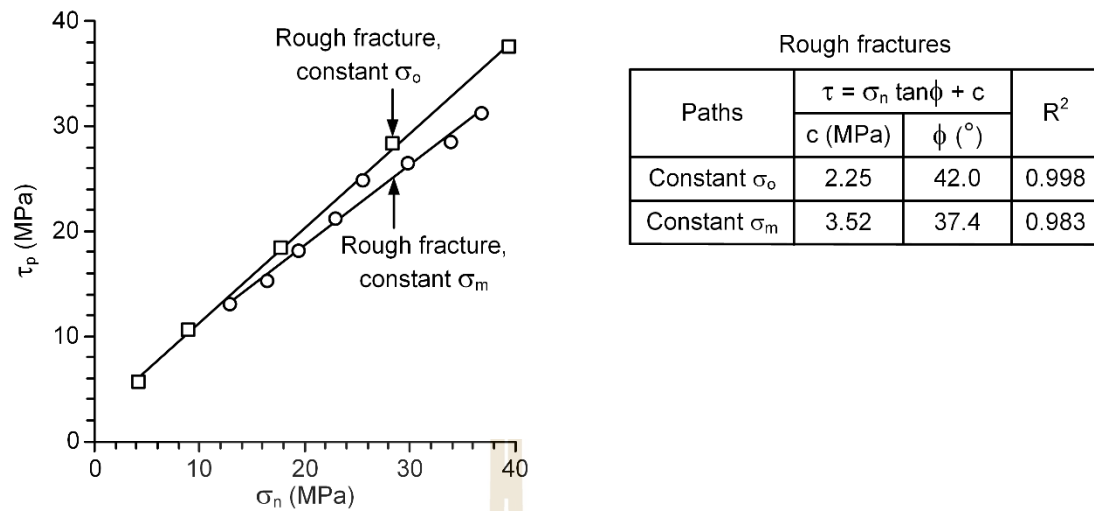
Figure 5.3 Peak shear stresses (τ_p) as a function of normal stresses (σ_n) for triaxial shear tests on rough fractures.

5.3 Triaxial shear tests on smooth fractures

The triaxial shear test and calculation methods on smooth fractures are identical to those of rough fractures. Table 5.2 shows the calculation results for both stress paths. Figure 5.4 shows the shear strengths as a function of normal stresses on smooth surface for both stress paths. The linear relation of the τ-σ_n line is observed. The Coulomb criterion using Equation (5.1) is applied to represent the results. Good correlations are obtained ($R^2 > 0.9$). The basic friction angle (ϕ_b) of smooth fractures for the constant σ_o and σ_m paths are determined as 32.3° and 31.0°, and the cohesion (c_b) are 0.40 and 0.50 MPa. The shear strengths for smooth fractures obtained from both stress paths are virtually identical, suggesting that stress path have insignificant impact on their shearing behavior. The shear strength thereby tends to pronounce with the roughness of the fracture.

Table 5.2 Summary of peak strengths and their corresponding normal stresses for smooth fractures.

Paths	σ_o (MPa)	$\sigma_{1,p}$ (MPa)	σ_n (MPa)	τ_p (MPa)
Constant σ_o	1.00	4.13	1.78	1.35
	3.00	11.01	5.00	3.47
	7.00	25.80	11.70	8.14
	12.00	41.28	19.32	12.68
	18.00	60.20	28.55	18.27
Constant σ_m	9.96	30.96	15.21	9.10
	11.34	39.56	18.40	12.22
	14.45	46.44	22.45	13.85
	15.84	53.32	25.21	16.23
	18.95	60.20	29.26	17.86
	21.30	68.80	33.17	20.57
	24.41	75.68	37.23	22.20
	25.79	84.28	40.42	25.32
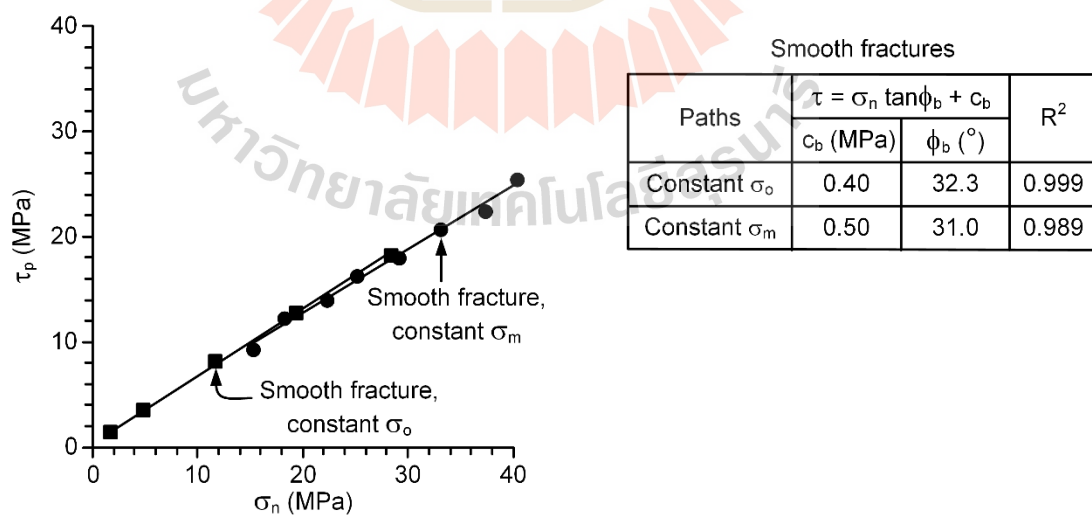
Figure 5.4 Peak shear stresses (τ_p) as a function of normal stresses (σ_n) for triaxial shear tests on smooth fractures.

5.4 Direct shear test results on rough fracture

The direct shear tests are performed for constant σ_n and τ paths. The primary objective of this test is to provide the shear strength results for different stress paths under low normal load. The results are presented in form of shear stresses-displacements (τ-d_s) curves and shear strengths-normal stresses (τ-σ_n) curves.

5.4.1 Shear stresses-displacements curves

The τ as a function of d_s of rough fracture are shown in Figure 5.5. Higher normal stresses are applied, higher shear stresses are obtained. The d_s of the peak stress under constant σ_n path is less than 1 mm and for constant τ path is less than 0.1 mm. The fracture displacements for the constant τ testing are obviously smaller than those of constant σ_n testing.
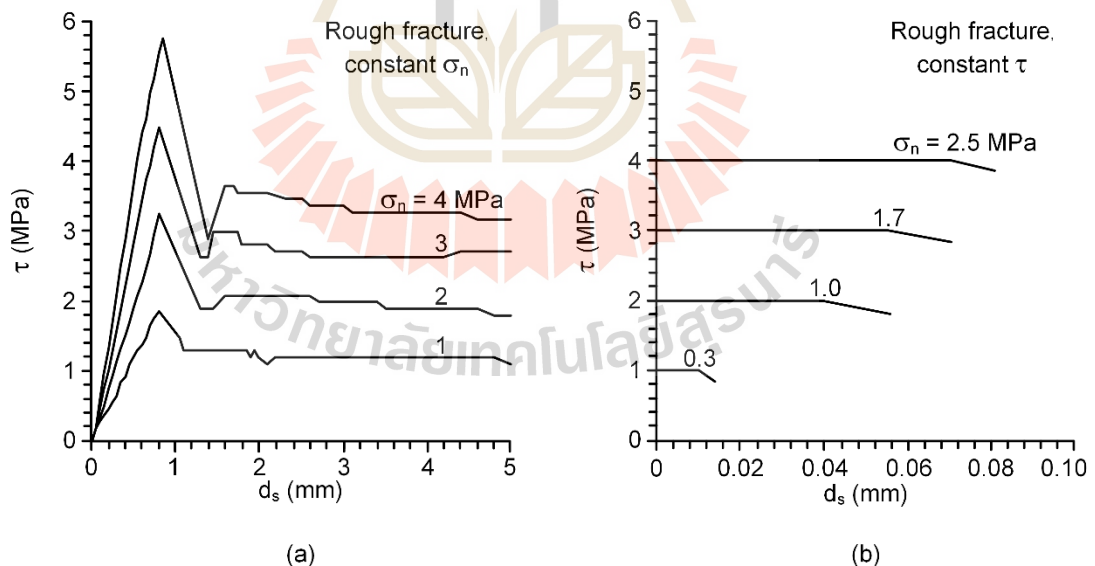
Figure 5.5 Shear stresses (τ) as a function of shear displacements (d_s) for direct shear tests on rough fractures under constant normal stress (a) and constant shear stress (b).

5.4.2 Shear strengths-normal stresses curves

The shear strengths as a function of normal stresses are shown in Figure 5.6. The linear relation is observed. Based on Coulomb criterion using Equation (5.1), the criterion fits well to all strength results, as suggested by their good correlation ($R^2 > 0.9$). The friction angle (ϕ) for constant σ_n and constant τ paths are determined as 52.0° and 53.8°. The cohesion (c) for constant σ_n and constant τ paths are determined as 0.64 and 0.62 MPa.

The strength results from both stress paths of the direct shear test are very similar. This suggests that under low normal stresses and unconfined condition the effect of stress path may not exist, which agrees with the shear strength results obtained from the triaxial shear tests under low confinement with different stress paths.

Paths	$\tau = \sigma_n \tan\phi + c$		R^2
	c (MPa)	ϕ (°)	
Constant σ_n	0.64	52.0	0.999
Constant τ	0.62	53.8	0.998
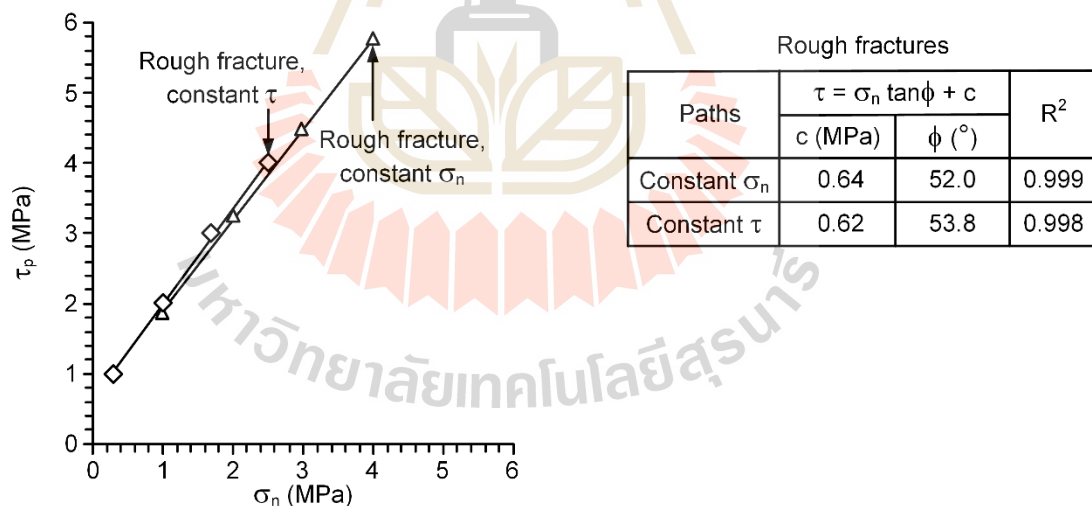
Figure 5.6 Shear strengths (τ) as a function of normal stresses (σ_n) on rough fractures for direct shear tests.

5.5   Fracture dilation

Dilation of the rough fracture is the normal separation of the fractures walls, induced by shearing movement of the fracture. The amount of the dilation is covered by the roughness of fracture, joint wall compressive strength and normal stress. The assessment of stress path has been made. Figure 5.7 shows the d_o-d_1 curves monitored during the triaxial shear tests. The angle θ represents the angle between the applied major principal stresses (σ_1) and normal to the fracture plane. The shear and normal displacements of triaxial shear tests using Equations (4.3) and (4.4) are calculated from the relative vertical and lateral displacements of the two wedge blocks, as shown in
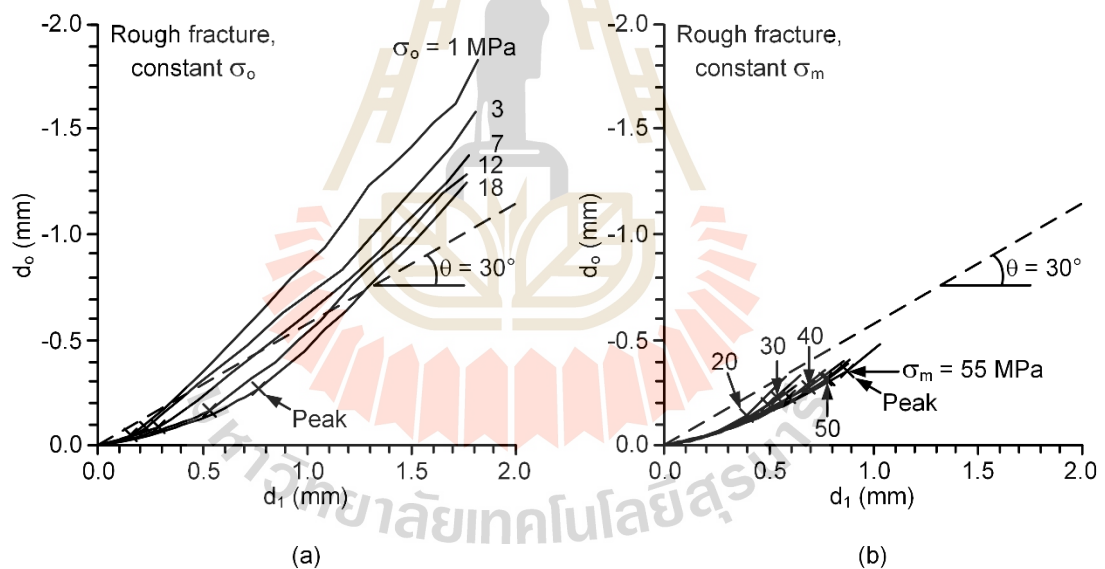
Figure 5.7   Lateral displacement (d_o) as a function of axial displacement (d_1) for triaxial shear tests under constant confining stress (a) and constant mean stress (b). Angle θ represents angle between axial dilation and fracture plane used in all triaxial test specimens. Cross signs ($\times$) represent dilations that correspond to peak stress.

Figure 5.8. Higher confinements induce lower fracture dilations which agrees with the test results obtained by Kleepmek et al. (2016). The fracture deformations obtained from triaxial shear tests are under compaction until peak shear stresses occur. Subsequently their movements tend to dilate. The normal and shear displacements (d_n-d_s) obtained from direct shear tests are presented in Figure 5.9. As the normal stress increases, the magnitude of dilation decreases significantly. For constant σ_n path all fracture deformations are similar to the triaxial shear tests above, except under σ_n of 3 and 4 MPa where the peak shear strengths are reached under dilation.
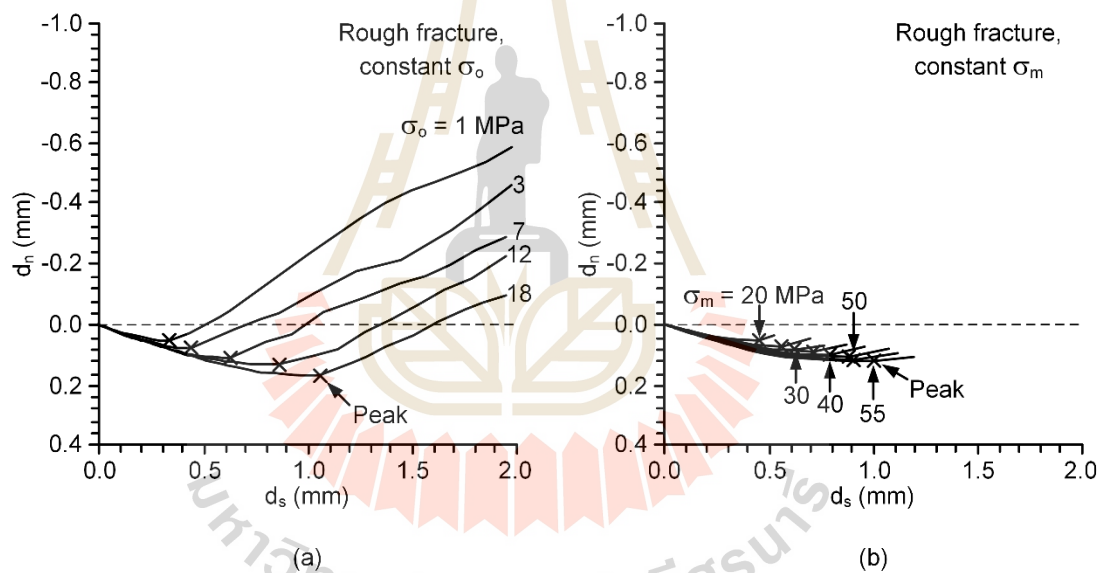
Figure 5.8 Normal displacements (d_n) as a function of shear displacements (d_s) for triaxial shear tests under constant confining stress (a) and constant mean stress (b). Cross signs ($\times$) represent dilations that correspond to peak stress.

The fracture dilation rates (d_n/d_s) measured near the peak stresses tend to decrease as the normal stresses increase, as shown in Figure 5.10. This is presumably because the joint walls climb over the asperities while shearing under low confining stresses (low normal stresses). They however tend to shear through the asperities under high confining stresses.

For the smooth fractures, there is no distinctive difference between the sheared-off surfaces observed before and after testing.
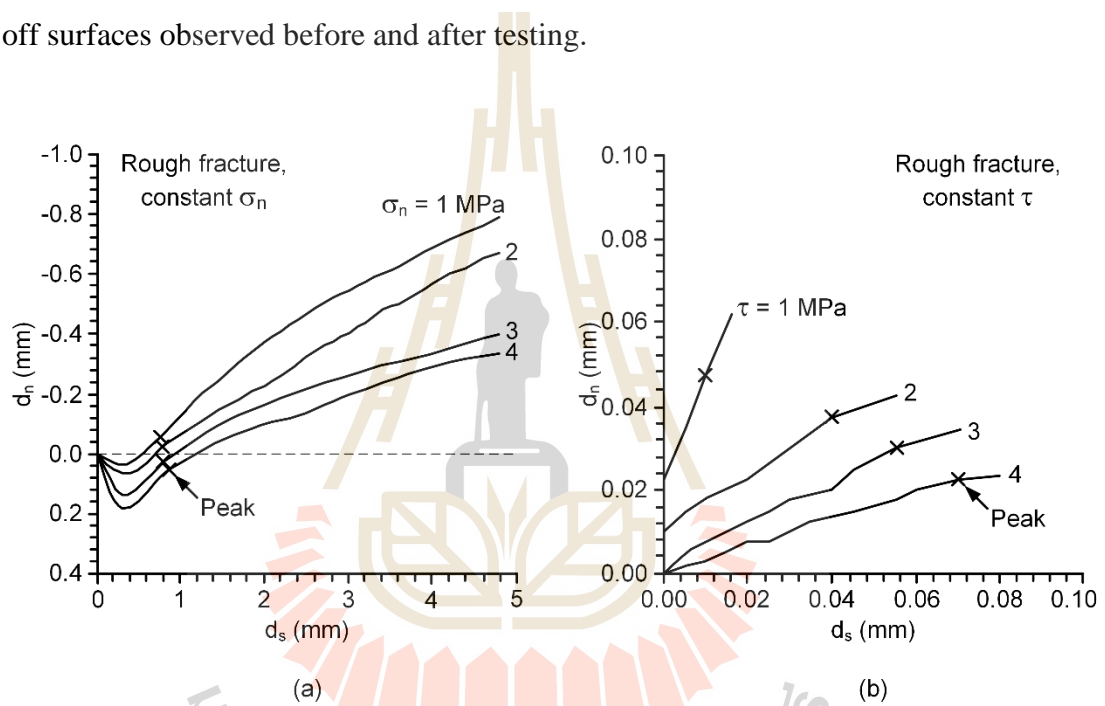
Figure 5.9 Normal displacements (d_n) as a function of shear displacements (d_s) for direct shear tests under constant normal stress (a) and under constant shear stress (b). Cross signs ($\times$) represent dilations that correspond to peak stress.
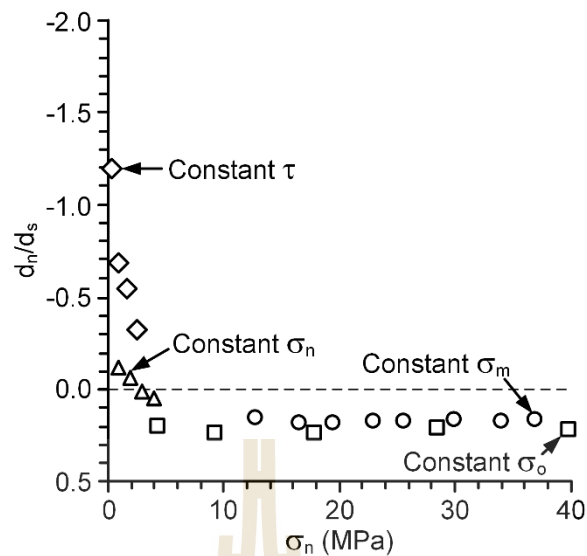
Figure 5.10 Fracture dilation rates (d_n/d_s) as a function of normal stresses (σ_n).

5.6 Post-test observations

Post-test fractures have been examined in attempt to qualitatively correlate the sheared-off areas with the confinements and stress path effect. A difficulty arises for this task. The post-test fractures are obscured by the deposition of the rock powder (gouges) resulting from the crushing of the asperities. Additionally, the shear displacements of after the tests are different of all stress paths. Tables 5.3 and 5.4 show examples of the post-test fractures, for the lowest to highest confinements for triaxial shear and direct shear tests. In the figure the light areas represent the sheared-off asperities with slight amount of gouge deposition. The post-test specimens for triaxial shear tests have usually been broken around the edges. Obtaining the laser scan results along the same profile as that obtained before testing is virtually impossible. This is more difficult by the relatively poor precision of the setting procedure of the available surface scanner. Nevertheless, some conclusions can be drawn. As expected, the increase of the confinements significantly increases the sheared-off areas for both stress

paths. This agrees reasonably well with the fracture dilation measured during the test (Figures 5.8 and 5.9).

Table 5.3 Post-test of rough fractures for triaxial shear test.

Table 5.4 Post-test of rough fractures for direct shear test.

Constant σ_n path	τ=1 MPa $\quad$ 2 MPa 3 MPa $\quad$ 4 MPa
constant τ path	σ_n=1 MPa $\quad$ 2 MPa 3 MPa $\quad$ 4 MPa

CHAPTER VI

STRAIN ENERGY DENSITY OF FRACTURES

6.1   Introduction

The strain energy density principle is applied to describe the fracture strength and deformation under different stress paths. It would be more comprehensive than other strength criteria because it considers both stress and stain at failure.

6.2   Strain energy density

The strain energy density principle is proposed to describe fracture shear strengths under both stress paths. It considers both stress and displacement at failure, and hence allows a more rigorous assessment of the sheared fracture behavior. The distortional (W_d) and mean (W_m) strain energy can be calculated from the test results as (Khamrat et al., 2018):

$$W_d = 3/2 \ \tau_{oct} \cdot \gamma_{oct} \tag{6.1}$$

$$W_m = 3/2 \ \sigma_m \cdot \varepsilon_m \tag{6.2}$$

where τ_{oct} and γ_{oct} are octahedral shear stress and strain, and σ_m and ε_m are mean stress and mean strain. The octahedral shear stress and mean stress can be calculated from the test results as follow:

$$\tau_{oct} = (1/3) \, [(\sigma_1 - \sigma_p)^2 + (\sigma_p - \sigma_o)^2 + (\sigma_o - \sigma_1)^2]^{1/2} \tag{6.3}$$

$$\sigma_m = (\sigma_1 + \sigma_p + \sigma_o) \, / \, 3 \tag{6.4}$$

Note that the strain that is parallel to the fracture strike is equal to zero ($\sigma_p = 0$) because the test configurations (loading platens) do not allow lateral displacement in this direction. As a result, the octahedral shear strain and mean strain at the peak point can be determined as follow:

$$\gamma_{oct} = (1/3) \, [\varepsilon_1{}^2 + \varepsilon_o{}^2 + (\varepsilon_1 - \varepsilon_o)^2]^{1/2} \tag{6.5}$$

$$\varepsilon_m = (\varepsilon_1 + \varepsilon_o) \, / \, 3 \tag{6.6}$$

where σ_1, σ_p and σ_o are the axial principal stresses and stresses that parallel and normal to fracture plane at the peak point, and ε_1 and ε_o are the axial and normal principal strains. Assuming that the intact portion of the specimen is rigid, the axial and lateral strains can be measured from the fracture displacements:

$$\varepsilon_1 = d_1 \, / \, L \tag{6.7}$$

$$\varepsilon_o = d_o \, / \, W \tag{6.8}$$

where d_1 and d_o are the axial and lateral displacements normal to the fracture strike, L is the specimen length (87 mm), and W is the specimen width (50 mm). Tables 6.1 and 6.2 give the distortional and mean strain energy calculated for the rough and smooth fractures for the two stress paths.

With reference to Tables 6.1 and 6.2, the results can be presented in Figures 6.1 and 6.2. The relations indicate that the distortional strain energy linearly increases with the mean strain energy for both stress paths which can be represented by:

$$W_d = A \, W_m + B \tag{6.9}$$

$$W_d = C \, W_m + D \tag{6.10}$$

where A, B, C and D are empirical parameters for the rough and smooth fractures. The distortional strain energy represents the deviatoric stresses that cause the shear displacement. The mean strain energy causes volume change and this can be related to the depth of the fractures. Regression analysis of the results of rough fractures against Equation (6.9) indicates that energy ratio of W_d to W_m, value (A) equal to 3.95 for the constant σ_m and 4.80 for the constant σ_o testing, as shown in Figure 6.1. The proposed criterion fits well to the test data with the correlation coefficient (R^2) greater than 0.9. As indicated above, under constant σ_m path the rough fracture yields lower value than those of the constant σ_o path. It is found that rougher fractures would give higher the energy ratio than that of smoother fractures. This agrees with test results obtained from Khamrat et al. (2018). For the rough fracture the energy ratio under the constant σ_o testing here is higher than those of results obtained by Khamrat et al. (2018) who adopted the results of displacement rate effects from Kleepmek (2014) to calculate the energy ratio on fracture in Phra Wihan sandstone. It is primarily because that the average JRC here of 8 is higher than those of their sandstone which equals to 6. For smooth fractures, as shown in Figure 6.2, their calculated energy densities are coincided and can be represented by a single failure envelope. The smooth fractures would

represent the lower bound of the energy required to shear the rock fractures. The upper

bound of energy ratio would be limited by that of the intact rock.

The strain energy density criterion explicitly considers both octahedral shear

stress and strain. Hence it can describe the fracture dilation as affected by stress paths

more comprehensively than the criterion developed in the previous in the Chapter V.

Table 6.1 Distortional and mean strain energy densities of rough fractures under different stress paths.

Paths	σ_p (MPa)	σ_o (MPa)	$\sigma_{1,p}$ (MPa)	d_1 (mm)	d_o (mm)	ε_1 ($\times 10^{-3}$)	ε_o ($\times 10^{-3}$)	W_d (MPa)	W_m (MPa)
Constant σ_o	1.00	1.00	13.87	0.300	-0.115	3.448	-2.300	0.021	0.003
	3.00	3.00	27.52	0.390	-0.135	4.483	-2.700	0.051	0.010
	7.00	7.00	49.66	0.550	-0.190	6.322	-3.800	0.126	0.027
	12.00	12.00	77.32	0.750	-0.280	8.621	-5.600	0.270	0.051
	18.00	18.00	104.56	0.920	-0.335	10.575	-6.700	0.435	0.091
Constant σ_m	20.00	5.22	35.48	0.390	-0.165	4.483	-3.300	0.059	0.012
	25.00	7.59	42.72	0.485	-0.195	5.575	-3.900	0.084	0.021
	30.00	8.87	50.72	0.540	-0.215	6.207	-4.300	0.111	0.028
	35.00	10.59	59.49	0.615	-0.250	7.069	-5.000	0.148	0.036
	40.00	11.12	68.40	0.685	-0.280	7.874	-5.600	0.194	0.045
	45.00	14.49	75.60	0.760	-0.315	8.736	-6.300	0.231	0.055
	50.00	17.28	83.29	0.780	-0.315	8.966	-6.300	0.253	0.067
	55.00	18.74	90.66	0.865	-0.360	9.943	-7.200	0.310	0.075

Table 6.2 Distortional and mean strain energy densities of smooth fractures under different stress paths.

Paths	σ_p (MPa)	σ_o (MPa)	$\sigma_{1,p}$ (MPa)	d_1 (mm)	d_o (mm)	ε_1 ($\times 10^{-3}$)	ε_o ($\times 10^{-3}$)	W_d (MPa)	W_m (MPa)
Constant σ_o	1.00	1.00	4.13	0.500	-0.170	5.747	-3.400	0.008	0.002
	3.00	3.00	11.01	0.535	-0.180	6.149	-3.600	0.023	0.007
	7.00	7.00	25.80	0.590	-0.180	6.782	-3.600	0.057	0.021
	12.00	12.00	41.28	0.650	-0.190	7.471	-3.800	0.097	0.040
	18.00	18.00	60.20	0.750	-0.217	8.621	-4.340	0.161	0.069
Constant σ_m	20.00	9.96	30.96	0.580	-0.215	6.667	-4.300	0.058	0.024
	25.00	11.34	39.56	0.620	-0.225	7.126	-4.500	0.083	0.033
	30.00	14.45	46.44	0.670	-0.240	7.701	-4.800	0.101	0.044
	35.00	15.84	53.32	0.690	-0.245	7.931	-4.900	0.121	0.053
	40.00	18.95	60.20	0.710	-0.260	8.161	-5.200	0.139	0.059
	45.00	21.30	68.80	0.740	-0.270	8.506	-5.400	0.166	0.070
	50.00	24.41	75.68	0.780	-0.280	8.966	-5.600	0.188	0.084
	55.00	25.79	84.28	0.800	-0.285	9.195	-5.700	0.220	0.096
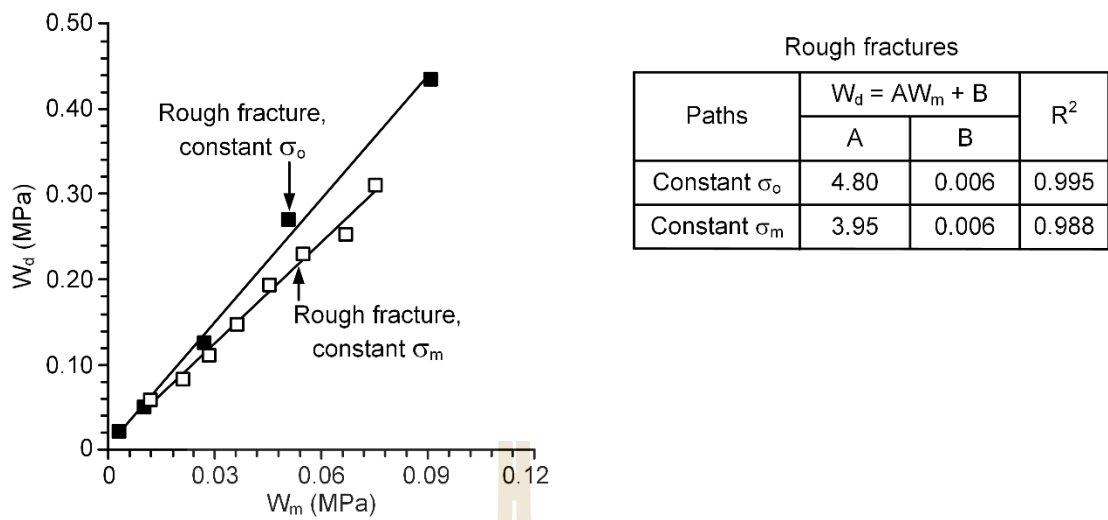
Figure 6.1 Distortion strain energy density (W_d) as a function of mean strain energy density (W_m) for rough fractures.
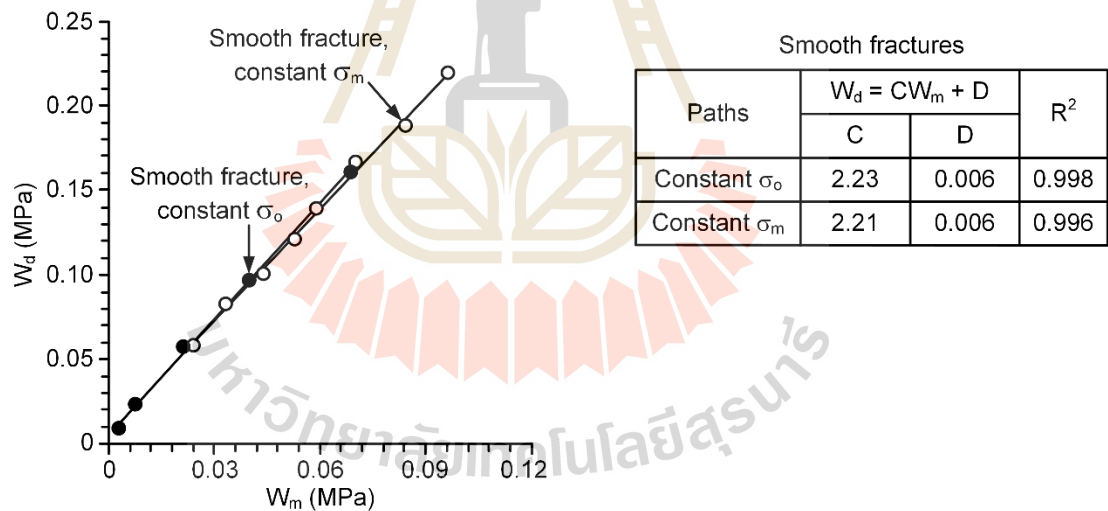
Figure 6.2 Distortion strain energy density (W_d) as a function of mean strain energy density (W_m) for smooth fractures.

6.3 Potential Applications

An attempt has been made at deriving the criterion that can be used to predict the fracture failure adjacent to an underground opening. A circular borehole is placed

in a homogeneous, isotopic, linear elastic material and in which the discontinuities (e.g. bedding planes, joint sets) are spaced and compressed under vertical (σ_v) and horizontal (σ_H, σ_h) principal stresses. The vertical opening is unsupported (internal pressure equal to zero). The vertical opening is located with varying a depth (z) up to 1,000 m. The estimated in-situ stresses are proposed by Brady and Brown (2004) as follow:

$$\sigma_v = 0.027 \cdot z \qquad (6.11)$$

$$\sigma_H = k \cdot \sigma_v \qquad (6.12)$$

where z is depth below the ground surface (m), σ_v is vertical principal stress (MPa), σ_H is maximum horizontal principal stress (MPa), and σ_h is minimum horizontal principal stress (MPa). The upper bound of ratio average of σ_H to σ_v (Brady and Brown, 2004) is defined as:

$$k = (1500/z) + 0.3 \qquad (6.13)$$

The parameter, k, can efficiently be described the in-situ states of stress at the depth over of 600 m. The calculation stresses are summarized in Table 6.3. For a design the relationship between the horizontal stress in direction of σ_H is two times the horizontal stress in direction of σ_h. Note that the orientation of σ_h with respect to magnetic north of 0º. Assuming that the orientations of joint sets are paralleled to the vertical opening, which those of the linear of joint sets are lied in the direction of 60º and 120º with respect to north, as shown in Figure 6.3. The blocks are identified the potential collapse with joint orientations and excavation surface of the vertical opening.

The cross sections of the blocks are generated around the vertical opening by symmetrically inclined joints.

The kirsch equations are a set of closed-form solutions, derived from the theory of elastic, used to calculate the stress around a circular excavation (Brady and Brown, 2004). The stress distributions around a borehole can be calculated by:

$$\sigma_r = \left(\frac{\sigma_H + \sigma_h}{2}\right)\left(1 - \frac{a^2}{r^2}\right) + \left(1 + \frac{3a^4}{r^4} - \frac{4a^2}{r^2}\right)\left(\frac{\sigma_H - \sigma_h}{2}\right)\cos 2\theta \qquad (6.14)$$

$$\sigma_\theta = \left(\frac{\sigma_H + \sigma_h}{2}\right)\left(1 + \frac{a^2}{r^2}\right) - \left(1 + \frac{3a^4}{r^4}\right)\left(\frac{\sigma_H - \sigma_h}{2}\right)\cos 2\theta \qquad (6.15)$$

where σ_θ and σ_r are tangential and radial principal stresses. a is borehole radius and r is radial distance from the center. Note that the strain parallel to the fracture strike is equal to zero (σ_v is constant). The stress components are calculated at the wall (r = a), which those are defined as:

$$\sigma_r = 0 \qquad (6.16)$$

Assuming that the fracture rock adjacent to the opening is a rigid body and the water pressure is absent. The principal stresses to the potential for collapse blocks A and B are summarized in Table 6.4.

Table 6.3 Summary of in-situ principal stresses at depth up to 1,000 m.

Depths (m)	σ_v (MPa)	k	σ_H (MPa)	σ_h (MPa)
600	16.2	2.8	45.36	22.68
700	18.9	2.4	46.17	23.09
800	21.6	2.2	46.98	23.49
900	24.3	2.0	47.79	23.90
1000	27.0	1.8	48.60	24.30
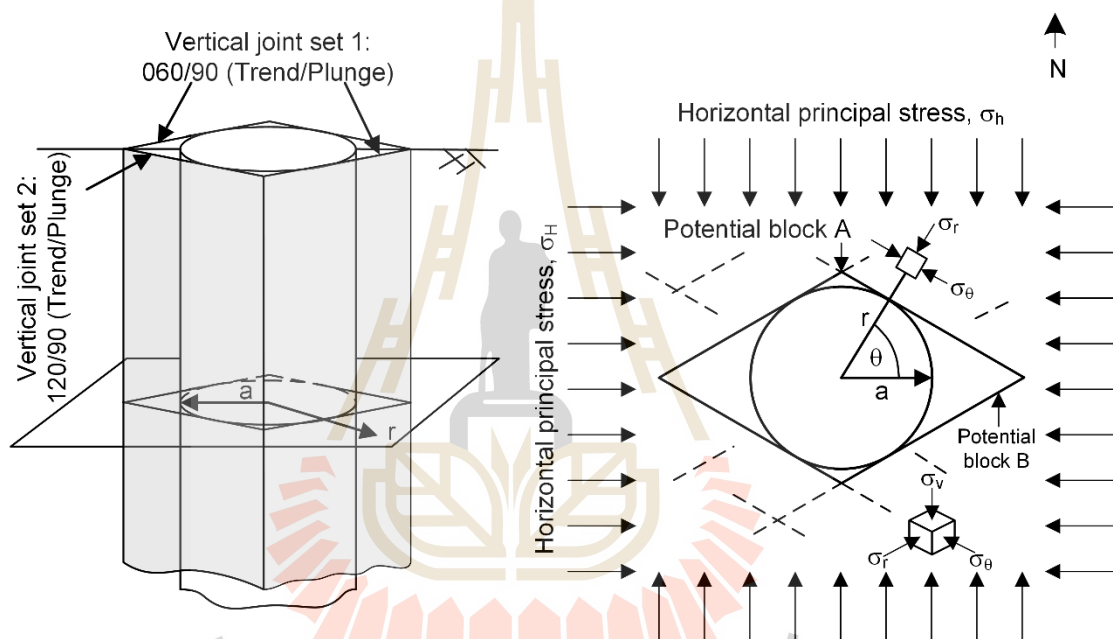
Figure 6.3 Principal stresses at wall of vertical shaft in an infinite rock mass.

6.3.1 Shear strength criterion

The stability of fracture, factor of safety (FS), can be determined by the ratio of the resisting force to the driving force (Duncan and Christopher, 2005), which it is defined as follows:

$$FS = \text{Resisting force} / \text{Driving force} \tag{6.17}$$

Table 6.4 Summary of principal stresses at blocks A and B at depth up to 1,000 m.

Depth (m)	σ_v (MPa)	σ_r (MPa)	σ_θ (MPa)	
			A (θ=90)	B (θ=0)
600	16.2	0	113.40	22.68
700	18.9	0	115.43	23.09
800	21.6	0	117.45	23.49
900	24.3	0	119.48	23.90
1000	27.0	0	121.50	24.30

Considering unit length of the block, the normal (N) and shear (S) forces act to the surface of fracture, as shown Figure 6.4. The shear and normal forces can be calculated as follow:

$$N = \sigma_\theta \sin \psi / R \tag{6.18}$$

$$S = \sigma_\theta \cos \psi / R \tag{6.19}$$

where ψ is angle of σ_θ direction to fracture plane. R is shear displacement in unit length. The resisting force (S_r) is expressed by substituting Equation (6.18) into Coulomb criterion as follows:

$$S_r = c/R + \sigma_\theta \sin \psi \tan \phi / R \tag{6.20}$$

The FS can be expressed by the resisting shear force and the driving shear force as follows:

$$FS = S_r / S \tag{6.21}$$

The FS can hence be calculated by substituting Equations (6.19) and (6.20) into Equation (6.21) as follows:

$$FS = (c + \sigma_\theta \sin \psi \tan \phi) / (\sigma_\theta \cos \psi) \tag{6.22}$$
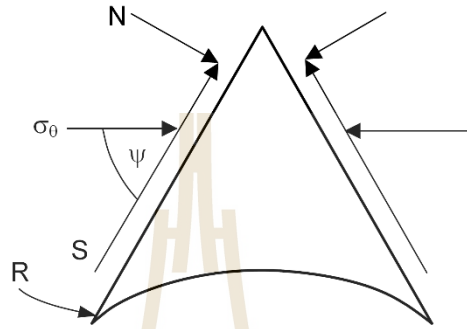
Figure 6.4 Free body diagram of block A under surface forces.

Method for analysis potential for block collapse B may be estimated by same variations in the proposed procedure of potential for block collapse A. The FS results for all potential failures with the Coulomb criteria are shown in Table 6.5. The FS values calculated from block A are lower than 1.0. For bock B, the FS values are higher than 1.0. The FS decreases slightly with increasing the depth. The criterion obtained from constant σ_o testing gives slightly higher FS than those of the constant σ_m testing. This suggests that the criterion obtained from constant σ_m testing is a more conservative estimation. With reference to the test results, stress path becomes insignificant when the normal stress is lower than 12.78 MPa. This suggests that the friction estimation of rock fracture for shallow underground structures, low normal stress, the criterion obtained from constant σ_o testing may be preferable.

Table 6.5 Summary of FS calculation results at wall of opening at depth up to 1,000

m using Coulomb criterion.

Collapse blocks	Paths	Depths (m)	N (MPa/m)	S_r (MPa/m)	S (MPa/m)	FS = S_r/S
A	Constant σ_o	600	56.70	53.33	98.21	0.543
		700	57.71	54.25	99.96	0.543
		800	58.73	55.16	101.71	0.542
		900	59.74	56.07	103.47	0.542
		1000	60.75	56.98	105.22	0.542
	Constant σ_m	600	56.70	46.82	98.21	0.477
		700	57.71	47.59	99.96	0.476
		800	58.73	48.37	101.71	0.476
		900	59.74	49.14	103.47	0.475
		1000	60.75	49.91	105.22	0.474
B	Constant σ_o	600	19.64	19.95	11.34	1.759
		700	19.99	20.26	11.54	1.755
		800	20.34	20.58	11.75	1.752
		900	20.69	20.89	11.95	1.749
		1000	21.04	21.21	12.15	1.746
	Constant σ_m	600	19.64	18.52	11.34	1.633
		700	19.99	18.79	11.54	1.627
		800	20.34	19.05	11.75	1.622
		900	20.69	19.32	11.95	1.617
		1000	21.04	19.59	12.15	1.612

6.3.2 Strain energy density criterion

The elastic parameters of the rough fracture are determined from the linear portion of the stress-strain relation. Assuming that the specimen is isotopic, shear modulus (G) and bulk modulus (K) can be calculated as follow:

$$G = 1/2 \ (\tau_{oct}/\gamma_{oct}) \tag{6.23}$$

$$K = \sigma_m / 3\varepsilon_m \tag{6.24}$$

The distortional strain energy can be calculated from octahedral shear stress and shear modulus for each rock fractures as follows:

$$W_d = 3/4G \ (\tau_{oct}^2) \tag{6.25}$$

For the mean strain energy density can be calculated from the mean stress and bulk modulus of each rock fractures as follows:

$$W_m = \sigma_m^2 / 2K \tag{6.26}$$

Each block is simulated for both stress paths. The input elastic parameters for calculation are given in Table 6.6. The definition of the factor of safety is used to evaluate stability of fracture around the opening. The FS is defined as the ratio of the W_d of material to $W_{d,f}$ of fracture at the wall of opening:

$$FS = W_d/W_{d,f} \tag{6.27}$$

where W_d is distortional strain energy of material calculated from proposed criterion and $W_{d,f}$ is distortional strain energy calculated from Equation (6.25) under in situ states of stress.

The calculation results in terms of distortional strain energy at the wall of opening are summarized in Table 6.7. Block B only gives FS higher than 1.0. The comparison indicates that the FS values of W_d-W_m criterion tends to increase with increasing depth, but the FS obtained from τ-σ_n criterion tends to decrease. This may be due to the high deviatoric stresses induced from high stress ratio (see Table 6.3) at shallow opening. The W_d-W_m criterion obtained by constant σ_o testing gives the FS values slightly higher than those of constant σ_m testing. The W_d-W_m criterion for constant σ_m testing can nevertheless provide a more conservative estimation under most stress states.

Table 6.6 Property parameters of rough fracture used in calculations.

Parameters	Values	
	Constant σ_o	Constant σ_m
Shear modulus, G (MPa)	2229	2020
Bulk modulus, K (MPa)	8512	17439

Table 6.7 Summary of FS calculation results at wall of opening at depth up to 1,000

m using strain energy density criterion.

Collapse blocks	Paths	Depths (m)	W_m (MPa)	W_d (MPa)	$W_{d,f}$ (MPa)	FS = $W_d/W_{d,f}$
A	Constant σ_o	600	0.110	0.533	0.844	0.632
		700	0.118	0.573	0.860	0.666
		800	0.126	0.613	0.877	0.699
		900	0.135	0.655	0.894	0.732
		1000	0.144	0.698	0.913	0.765
	Constant σ_m	600	0.054	0.217	0.931	0.233
		700	0.057	0.233	0.949	0.245
		800	0.062	0.249	0.968	0.257
		900	0.066	0.266	0.987	0.269
		1000	0.070	0.283	1.008	0.281
B	Constant σ_o	600	0.010	0.054	0.031	1.753
		700	0.012	0.062	0.034	1.814
		800	0.013	0.070	0.038	1.833
		900	0.015	0.079	0.043	1.822
		1000	0.017	0.089	0.050	1.791
	Constant σ_m	600	0.005	0.025	0.034	0.740
		700	0.006	0.028	0.037	0.752
		800	0.006	0.032	0.042	0.749
		900	0.007	0.035	0.048	0.735
		1000	0.008	0.039	0.055	0.714

CHAPTER VII

DISCUSSIONS CONCLUSIONS AND

RECOMMENDATIONS FOR FUTURE STUDIES

7.1   Discussions

This chapter discusses the key issues relevant to the reliability of the test schemes and the adequacies of the test results. Comparisons of the results and findings from this study with those obtained elsewhere under similar test conditions are made.

According to the literature review, the effect of stress path is significant for inelastic materials. Phra Wihan sandstone is selected. It is classified based on ISRM (Hoek and Brown, 1997) as medium strong rock and with highly uniform texture. The relatively large crystal sizes of the rock forming minerals may promote the roughness of the fracture by line load method. The fracture roughness of the test specimens is controlled by petrographic characteristics of the rock (e.g. crystal, mineral composition, texture, etc.).

If the angle β is larger, the stress condition on the triaxial shear test specimens would be closer to those of the direct shear test. It is believed that if the angle is reduced to below 45° the shear sliding on the fractures may not occur, instead the compression failure of the intact rock wedge would take place. The angle β however should not affect the τ-σ_n relations.

The residual shear stress can not be obtained from the constant σ_m testing because the stress can not be maintained constant after the peak shear stress has been reached.

The number of the test specimens seem adequate, as evidenced by the good coefficients of correlation for all stress paths (see Figures 5.3, 5.4 and 5.6). The minimum magnitude of constant σ_o testing is limited by the capacity of the triaxial test frame. The shear strengths of the rough and smooth fractures can well be described by the Coulomb criterion.

The results clearly indicate that under high confinements the shear strengths of rough fractures under constant σ_m path is lower than those of the constant σ_o path. For intact rock, Mellegard and Pfeifle (1999), Weng and Ling (2013), and Artkhonghan and Fuenkajorn (2015) propose an explanation for the constant σ_m path that when σ_1 is increased as the σ_2 and/or σ_3 are decreased, the dilation occurs along the σ_2 and/or σ_3 directions. This makes the rocks fail more easily under constant σ_m path. This postulation can help explaining the discrepancy of the fracture shear strengths obtained under different stress paths here. Recognizing the effects of stress path on the fracture shear strength under high confining pressures would be useful to obtain a more conservative analysis and design of underground openings in rock mass.

The findings indicate that the rougher fractures, the more effect from the stress path is pronounced. This is evidenced by that the shear strength of the smooth fracture for triaxial shear tests is independent of the stress path, which agrees with the results obtained by Tisa and Kovari (1984) who perform different stress paths on smooth fractures in granite. Both stress paths from the direct shear testing yield similar shearing

resistance of the rough fractures. This is because the fractures are under low confinement.

The dilations measured prior to and after the peak shear stresses notably decrease with the large confinement (see Figures 5.8 and 5.9), as shown by the d_n/d_s-σ_n diagrams form (see Figure 5.10). The dilation rate, d_n/d_s, tends to decrease as the normal stresses increase. This is presumably because the joint walls climb over the asperities while shearing under low confining stress (low normal stresses). The asperities however are sheared though under high confining stresses. This is supported by the post-test observations.

The advantage of the application of stain energy density criterion over the shear strength criterion is that it considers both stress and strain at peak stress. Their results would hence be more comprehensive than the shear strength criterion. The distortional and mean strain energy densities are calculated from the test results. All deformations are from the shear and dilation within the fracture with the assumption that the rock adjacent to a fracture is rigid. The energy ratio obtained from the constant σ_m testing gives a lower value than those of the constant σ_o testing (see Figure 6.1). For smooth surface their linear relation has implicitly incorporated the effects of the stress paths (see Figure 6.2). The energy ratio depends on the fracture roughness and strength of the asperities. The energy ratio of the rough fractures is steeper than that of the smooth fracture, suggesting that higher strain energy is required to displace the rough fractures than the smooth ones.

It is not intended here that the W_d-W_m criterion is better than the τ-σ_n criterion. Depending on the site-specific requirements and load regulations. The stability of fractures may be estimated by any criteria.

It should be noted that construction of infrastructure acting on the fracture plane due to its weight yields similar stress path to constant σ_o testing. The criterion for constant σ_o testing will therefore be preferred to evaluate the stability of the fracture than other one.

For many rock cuts of block lying on the fracture plane could decrease weight of the block, which it provides to reduce simultaneously the shear and normal forces. Nevertheless, it is in fact evidence from the test results that strength of the fractures tends to be independent of stress path effect (see Figure 5.6). The conventional direct shear test, constant σ_n test, is preferred to describe in any condition of the man-made slopes near ground surface because it is simple and sufficient to generate the parameters of shear strength criterion.

7.2 Conclusions

All objectives and requirements of this study have been met. The results of the laboratory testing and analyses can be concluded as follow:

1. The τ-σ_n and W_d-W_m criteria under confinements of rough fractures for constant σ_m testing is lower than those of the constant σ_o testing (see Figures 5.3 and 6.1).

2. The smooth fracture is independent of the effect of stress path (see Figures 5.4 and 6.2).

3. Under low confinement, the rough fractures tend to be independent of the stress path (see Figure 5.6).

4. The shear strengths of the rough and smooth fractures can be well described by the Coulomb criterion. These equations can be used to determine the

stability of engineering structures (e.g. slope protection, foundation and tunnel) where applied shear and normal stress are known.

     5. The fracture dilations measured prior to and after the peak shear strengths significantly decrease with increasing confinements or normal stresses.

     6. The W_d-W_m criterion is more comprehensive than τ-σ_n criterion as it considers both stress and strain at failure. The W_d-W_m criterion obtained from constant σ_m testing can provide a more conservative estimation of a stability analyses (see Table 6.7).

## 7.3　Recommendations for future studies

     The fracture areas used in this study (100×50 mm^2 for triaxial shear tests and 100×100 mm^2 for direct shear tests) are relatively small even though they are well complied with the relevant standard practice and internationally suggested method (e.g. ASTM D5607-16). Testing on larger fracture areas would provide a more representative of the shear strength results when they are applied to the actual fractures under in-situ condition. The scale effect on the fracture shear strengths has also been addressed by Bandis et al. (1981) and Fardin et al. (2001).

     The shearing resistance under constant mean stress and fully saturated condition of rock specimen should be determined. The effect of water saturation on rock fracture under high pressure has been recognized by Stesky (1978) and Liapkrathok et al. (2018).

     Increasing the number of the specimens would statistically enhance the reliability of the test results and the predictability of the proposed criterion.

Performing the shear tests on a variety of rock types with different fractures, hardness and strengths would improve our understanding of the different stress path on the fracture shear strength. In particular the fractures prepared in time-dependent rock would reveal the strengths of the fracture rock wall as affected by the stress path. The knowledge on how the plastic or time-dependent rock wall fractures respond to the different stress paths would be benefit to understand the fractures behavior.

REFERENCES

Artkhonghan, K. and Fuenkajorn, K. (2015). Effects of stress path on polyaxial strengths of Maha Sarakham salt. **In Proceedings of the VietRock 2015 International Workshop - an ISRM Specialised Conference.** Hanoi, Vietnam.

ASTM D5607-16. (2016). **Standard Test Method for Performing Laboratory Direct Shear Strength Tests of Rock Specimens under Constant Normal Force.** In Annual Book of ASTM Standards. West Conshohocken, PA: American Society for Testing and Materials.

Bandis, S., Lumsden, A., and Barton, N. (1981). Experimental studies of scale effects on the shear behaviour of rock joints. **International Journal of Rock Mechanics and Mining Sciences and Geomechanics Abstracts.** 18(1): 1-21.

Barton, N. (1976). The shear strength of rock and rock joints. **International Journal of Rock Mechanics and Mining Sciences and Geomechanics Abstracts.** 13(9): 255-279.

Barton, N.R. (1982). Shear strength investigations for surface mining. In Brawner, C.O. (Ed.). **Proceedings of the Third International Conference on Stability in Surface Mining** (Ch. 7: pp. 171-196). Vancouver, British Columbia, Canada: New York: Society of Mining Engineers of AIME.

Beer, F.P., Johnston, E.R., DeWolf, J.T., and Mazurek, D.F. (2012). **Mechanics of Materials** (6th ed.). McGraw-Hill Education, New York.

Brady, B.H.G. and Brown, E.T. (2004). **Rock Mechanics for Underground Mining** (3rd ed.). Springer Publishing, New York.

Byerlee, J.D. (1967). Frictional characteristics of granite under high confining pressure. **Journal of Geophysical Research**. 72(14): 3639-3648.

Crouch, S.L. (1972). A note on post-failure stress-strain path dependence in norite. **International Journal of Rock Mechanics and Mining Sciences**. 9(2): 197-204.

Duncan, C.W. and Christopher, W.M. (2005). **Rock Slope Engineering: Civil and Mining** (4th ed.). Taylor & Francis, Abingdon, United Kingdom.

Fardin, N., Stephansson, O., and Jing, L. (2001). The scale dependence of rock joint surface roughness. **International Journal of Rock Mechanics and Mining Sciences.** 38(5): 659-669.

Fuenkajorn, K., Sriapai, T., and Samsri, P. (2012). Effects of loading rate on strength and deformability of Maha Sarakham salt. **Engineering Geology.** 135-136: 10-23.

Hoek, E. and Brown, E.T. (1997). Practical estimates of rock mass strength. **International Journal of Rock Mechanics and Mining Sciences.** 34(8): 1165-1186.

Hudson, J.A. and Harrison, J.P. (2002). Principal of the stress path and its visualization for rock mechanics and rock engineering. In **Proceedings of the Second International Conference on New Development in Rock Mechanics and Rock Engineering** (pp. 1-4). Shenyang, People's Republic of China.

Hudson, J.A., Cornet, F.H., and Christiansson, R. (2003). ISRM Suggested Methods for rock stress estimation—Part 1: Strategy for rock stress estimation. **International Journal of Rock Mechanics and Mining Sciences.** 40(7-8): 991-998.

Jaeger, J.C., Cook, N.G.W., and Zimmerman, R.W. (2007). **Fundamentals of Rock Mechanics** (4th ed.). Blackwell Publishing, Malden, Massachusetts.

Jeng, F.S., Weng, M.C., Huang, T.H., and Lin, M.L. (2002). Deformational characteristics of weak sandstone and impact to tunnel deformation. **Tunnelling and Underground Space Technology.** 17(3): 263-274.

Jin-feng, C., Ming, X., Er-xiang, X., and Guang-xu, C. (2012). Large scale triaxial testing on mechanical properties of broken limestone under various stress paths. **Engineering Mechanics.** 29: 8.

Kapang, P., Walsri, C., Sriapai, T., and Fuenkajorn, K. (2013). Shear strengths of sandstone fractures under true triaxial stresses. **Journal of Structural Geology.** 48: 57-71.

Kenter, C.J., Brignoli, M., and Holt, R.M. (1997). CMS (constant mean stress) VS. UCS (unconfined strength) tests: A tool to reduce core damage effects. **International Journal of Rock Mechanics and Mining Sciences.** 34(3-4).

Khamrat, S., Archeeploha, S., and Fuenkajorn, K. (2016). Pore pressure effects on strength and elasticity of ornamental stones. **ScienceAsia.** 42(2): 121-135.

Khamrat, S., Thongprapha, T., and Fuenkajorn, K. (2018). Thermal effects on shearing resistance of fractures in Tak granite. **Journal of Structural Geology.** 111: 64-74.

Kleepmek, M. (2014). **Effects of Shear Velocity of Fracture Shear Strength of Rocks under Confinements.** PhD. Thesis, Suranaree University of Technology, Nakhon Ratchasima, Thailand.

Kleepmek, M., Khamrat, S., Thongprapha, T., and Fuenkajorn, K. (2016). Displacement velocity effects on rock fracture shear strengths. **Journal of Structural Geology.** 90: 48-60.

Komenthammasopon, S. (2014). **Effects of Stress Path on Rock Strength under True Triaxial Condition.** Master Thesis, Suranaree University of Technology, Nakhon Ratchasima, Thailand.

Liapkrathok, P., Khamrat, S., Thongprapha, T., and Fuenkajorn, K. (2018). Shearing resistance of fractures in saturated Phra Wihan sandstone. **Engineering Journal of Research and Development.** 29(3): 37-46.

Martin, C.D. (1997). Seventeenth Canadian geotechnical colloquium: the effect of cohesion loss and stress path on brittle rock strength. **Canadian Geotechnical Journal.** 34(5): 698-725.

Maurer, W.C. (1965). Shear failure of rock under compression. **Society of Petroleum Engineers Journal.** 5(2): 167-176.

Mellegard, K.D. and Pfeifle, T.W. (1999). Laboratory evaluation of mechanical properties of rock using an automated triaxial compression test with a constant mean stress criterion. In Marr W.A. and Fairhurst C.E., (Eds.). **Nondestructive and Automated Testing for Soil and Rock Properties** (pp. 247-258). West Conshohocken, PA: ASTM STP 1350

Nai-guang, G., Yong, C., and Xiao-xin, Y. (1981). Stress paths and strength of rocks. **Acta Mechanica Sinica.** 5: 525-527.

Nai-guang, G., Jin-sheng, H., Ji-han, L., Xiao-hong, L., Yaru, F., and Daien, C. (1987). Stress path and frictional sliding of rock. **Acta Seismologica Sinica.** 9(2).

Orowan, E. (1960). Mechanism of seismic faulting. **Geological Society of America.** 79: 323-345.

Ramamurthy, T. and Arora, V. (1994). Strength predictions for jointed rocks in confined and unconfined states. **International Journal of Rock Mechanics and Mining Sciences and Geomechanics Abstracts.** 31(1): 9-22.

Sartkaew, S. and Fuenkajorn, K. (2013). Effects of stress rate on uniaxial compressive strength of rock salt under 0-100 C. In **Proceedings of the Eleventh International Conference on Minerals and Petroleum Engineering** (pp. 13-20). Chiang Mai, Thailand.

Sriapai, T., Walsri, C., and Fuenkajorn, K. (2012). Effect of temperature on compressive and tensile strength of salt. **ScienceAsia.** 38: 166-174.

Stesky, R. (1978). Rock friction-effect of confining pressure, temperature, and pore pressure. **Pure and Applied Geophysics.** 116(4): 690-704.

Swansson, S.R. and Brown, W.S. (1971). An observation of loading path independence of fracture in rock. **International Journal of Rock Mechanics and Mining Sciences**. 8(3): 277-281.

Tisa, A. and Kovári, K. (1984). Continuous failure state direct shear tests. **Rock Mechanics and Rock Engineering.** 17(2): 83-95.

Weng, M.C. and Ling, H.I. (2013). Modeling the behavior of sandstone based on generalized plasticity concept. **International Journal for Numerical and Analytical Methods in Geomechanics.** 37(14): 2154-2169.

Wu, W., Zhao, Z., and Duan, K. (2017). Unloading-induced instability of a simulated granular fault and implications for excavation-induced seismicity. **Tunnelling and Underground Space Technology.** 63: 154-161.

Wu, W., Zou, Y., Li, X., and Zhao, J. (2014). An unload-induced direct-shear model for granular gouge friction in rock discontinuities. **Review of Scientific Instruments.** 85(9).

Xiao-xin, Y., Nai-guang, G., and Yong, C. (1980). The effect of stress path on brittleness and ductility of rocks. **Acta Geophysica Sinica.** 23(3).

Yang, S.Q., Jing, H.W., and Wang, S.Y. (2012). Experimental investigation on the strength, deformability, failure behavior and acoustic emission locations of red sandstone under triaxial compression. **Rock Mechanics and Rock Engineering.** 45(4): 583-606.

Yang, S.Q., Jing, H.W., Li, Y.S., and Han, L.J. (2011). Experimental investigation on mechanical behavior of coarse marble under six different loading paths. **Experimental Mechanics.** 51(3): 315-334.

Zhao, J. (1997). Joint surface matching and shear strength part A: joint matching coefficient (JMC). **International Journal of Rock Mechanics and Mining Sciences.** 34(2): 173-178.

Zhao, X.G. and Cai, M. (2014). Influence of specimen height-to-width ratio on the strainburst characteristics of Tianhu granite under true-triaxial unloading conditions. **Canadian Geotechnical Journal.** 52(7): 890-902.
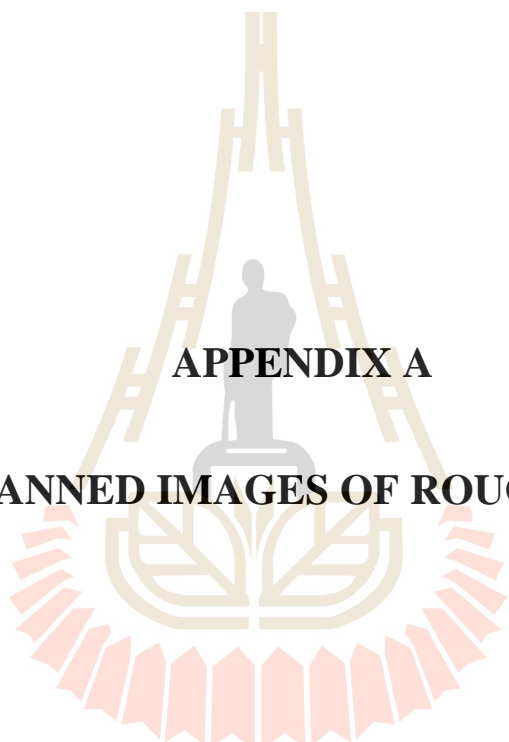
APPENDIX A

LASER SCANNED IMAGES OF ROUGH FRACTURE
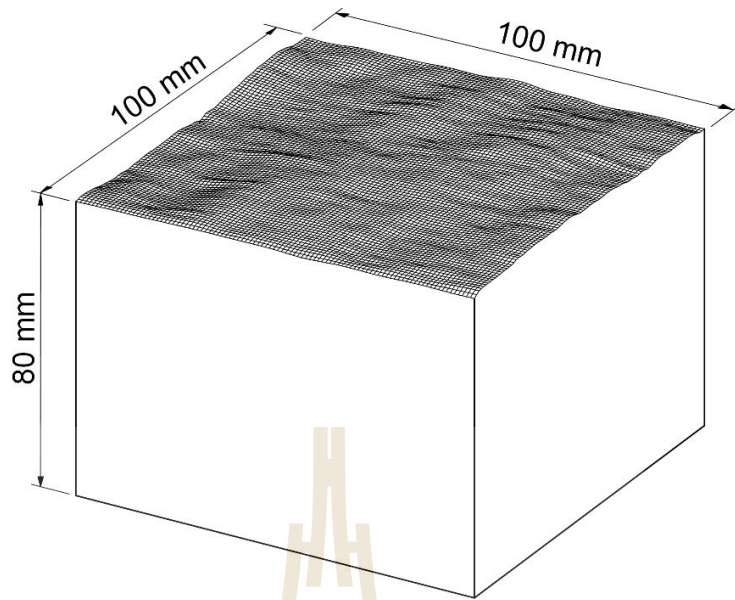
Figure A.1 Specimen No. CNS-PWS-TI-1.
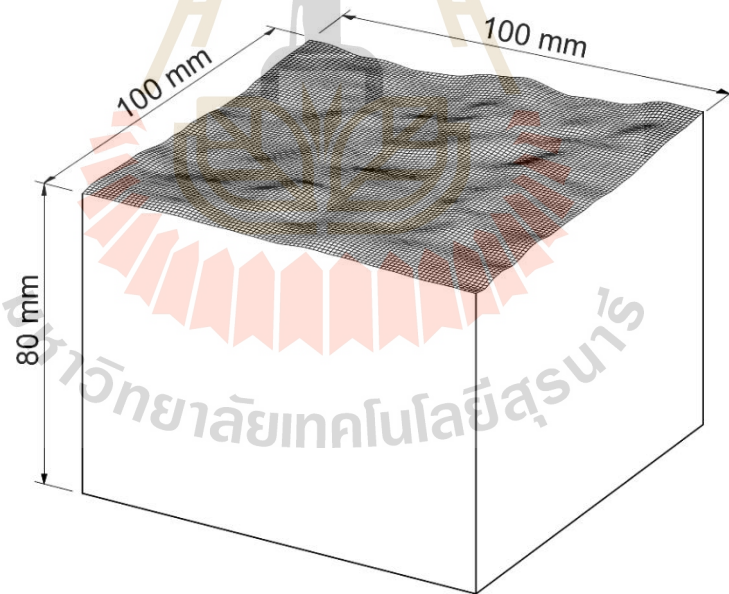
**Figure A.2** Specimen No. CNS-PWS-TI-2.
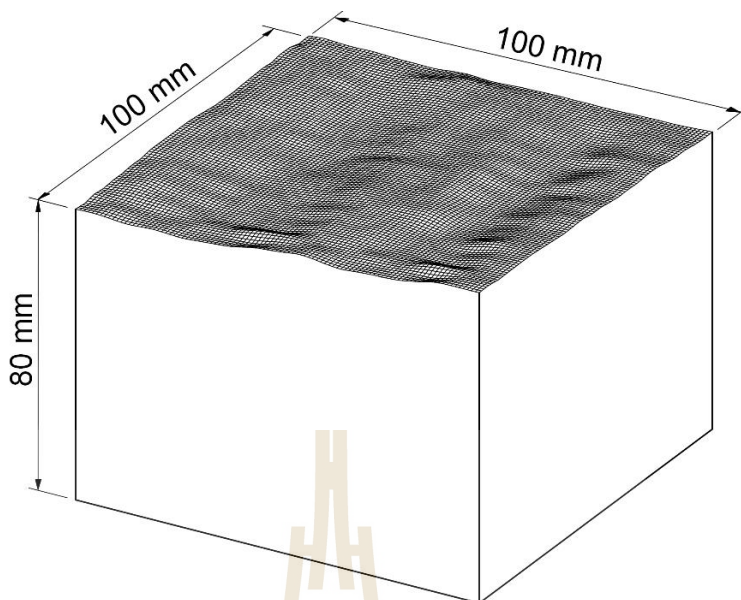
Figure A.3 Specimen No. CNS-PWS-TI-3.
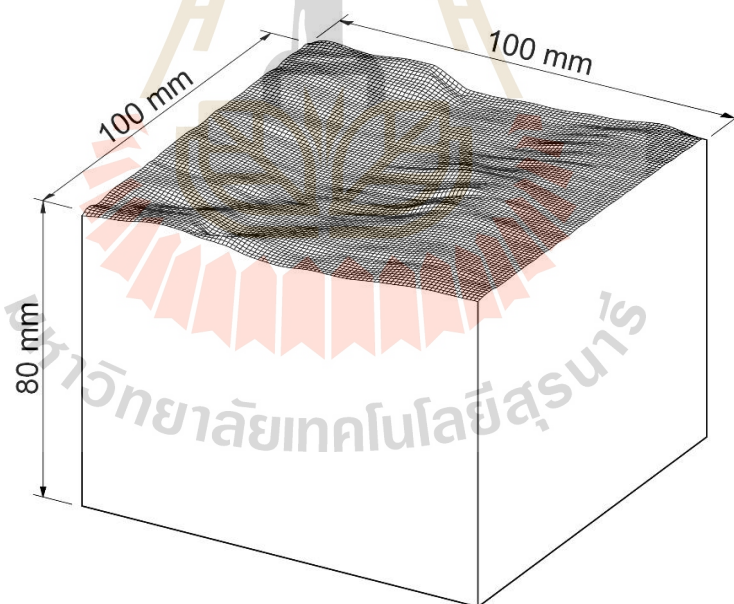
Figure A.4 Specimen No. CNS-PWS-TI-4.
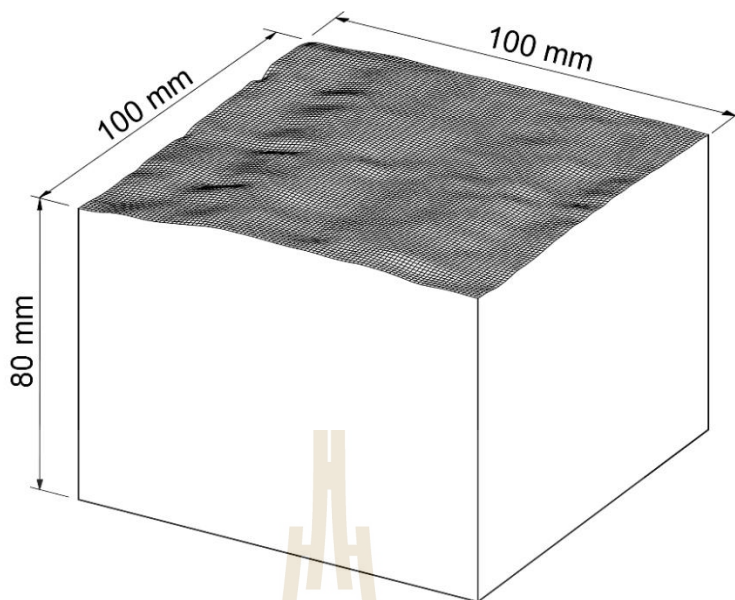
Figure A.5 Specimen No. CSS-PWS-TI-1.
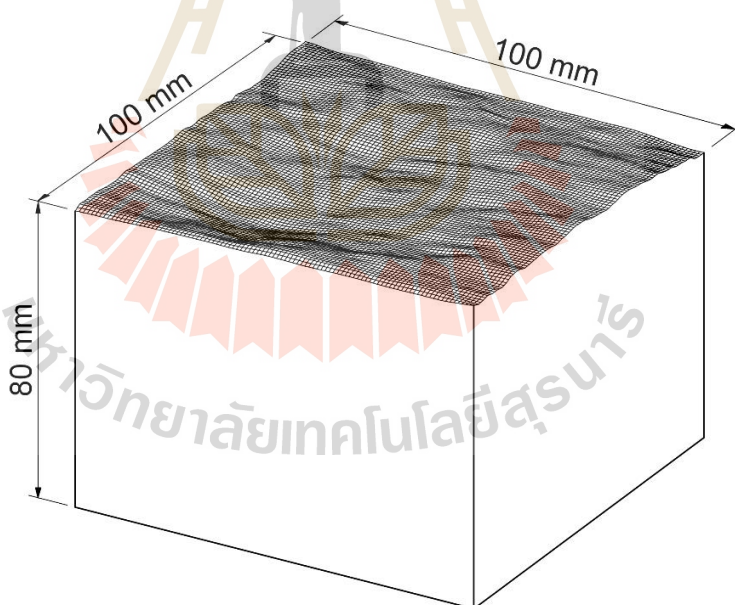

Figure A.6 Specimen No. CSS-PWS-TI-2.
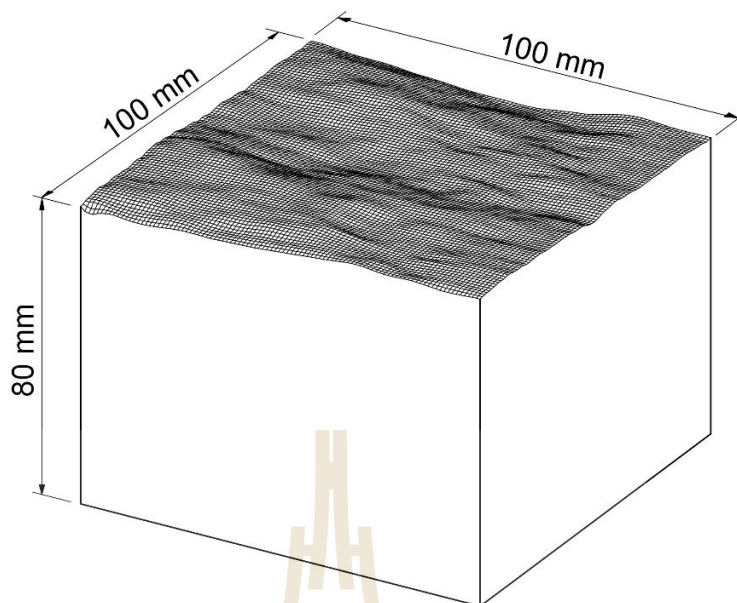
Figure A.7 Specimen No. CSS-PWS-TI-3.
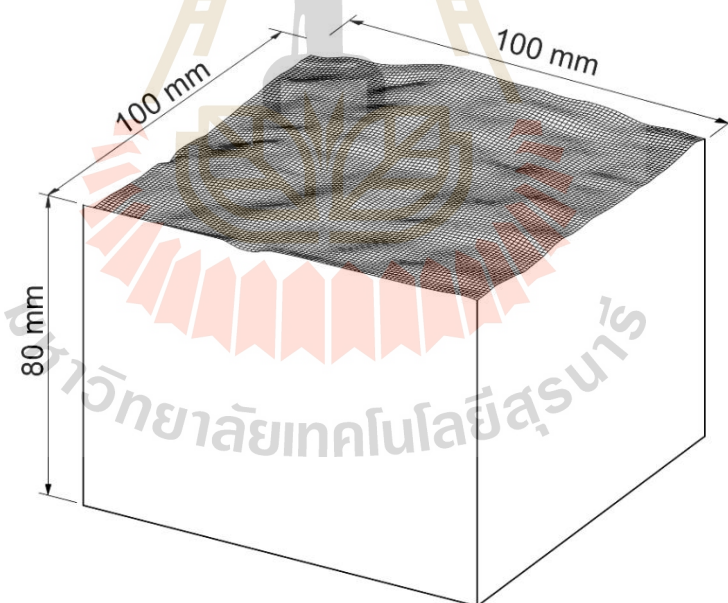
Figure A.8 Specimen No. CSS-PWS-TI-4.
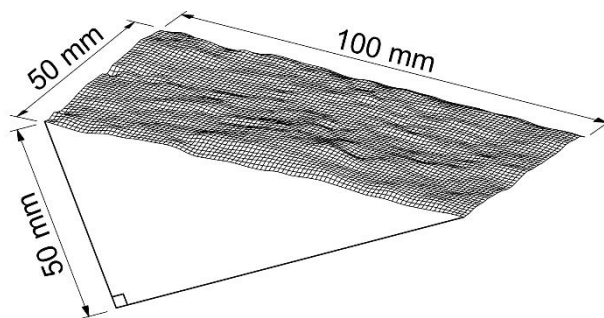
Figure A.9 Specimen No. CMS-PWS-TI-1.
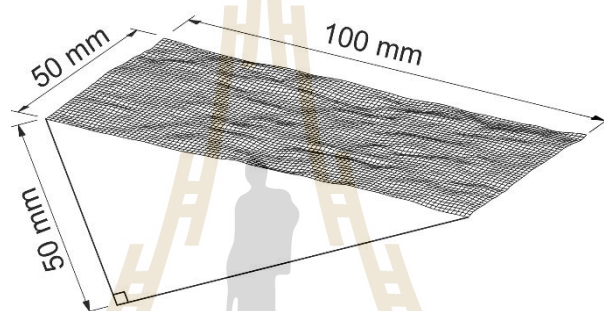

Figure A.10 Specimen No.CMS-PWS-TI-2.
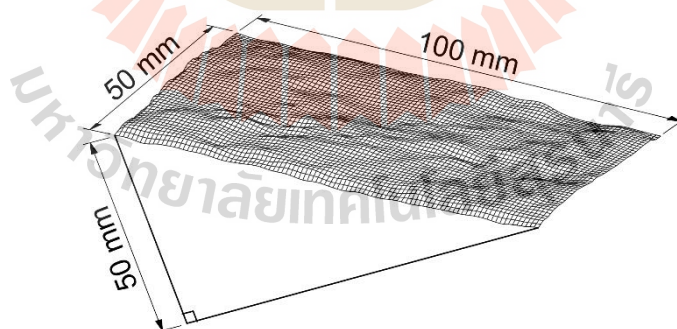
Figure A.11 Specimen No.CMS-PWS-TI-3.
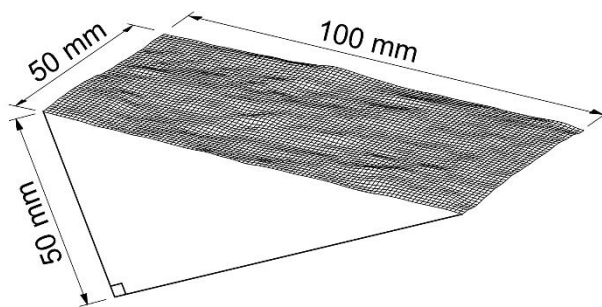
Figure A.12 Specimen No.CMS-PWS-TI-4.
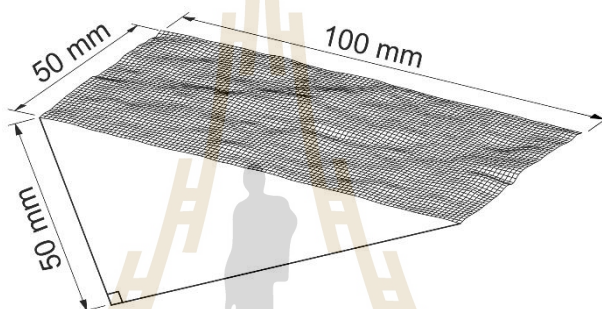
Figure A.13 Specimen No.CMS-PWS-TI-5.
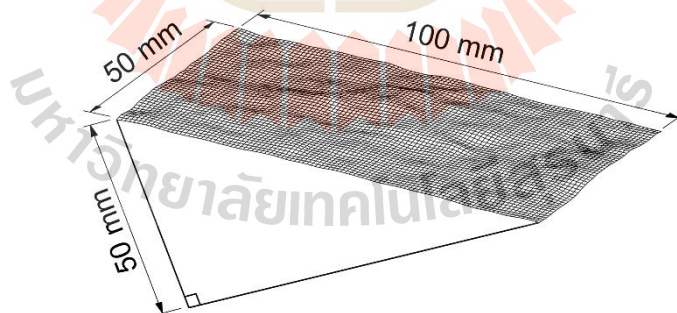
Figure A.14 Specimen No.CMS-PWS-TI-6.
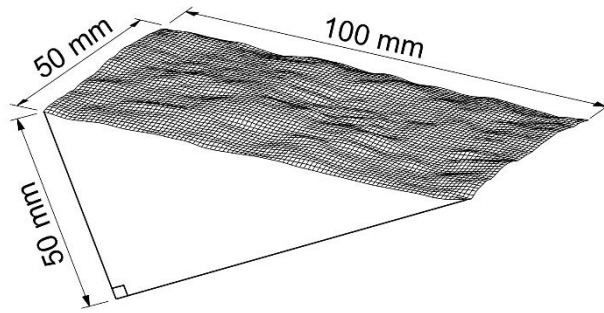
Figure A.15 Specimen No.CMS-PWS-TI-7.
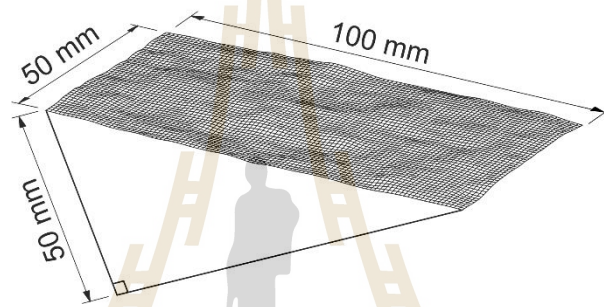
Figure A.16 Specimen No.CMS-PWS-TI-8.
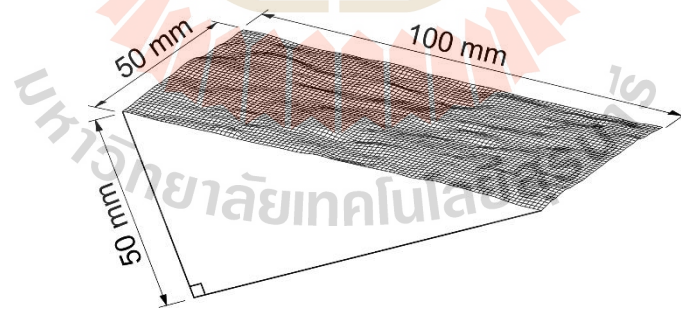
Figure A.17 Specimen No.CCS-PWS-TI-1.
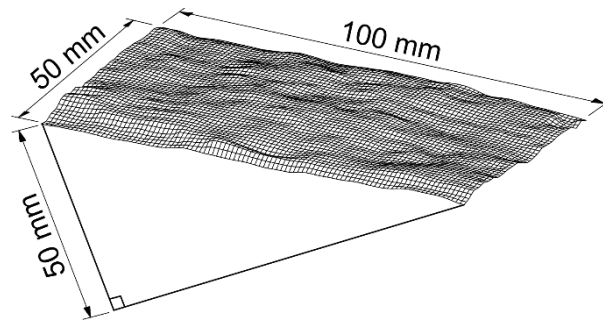
Figure A.18 Specimen No.CCS-PWS-TI-2.
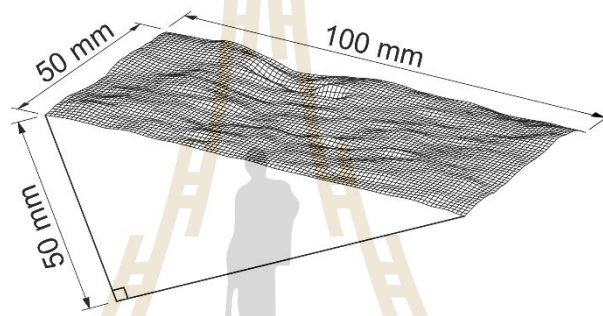
**Figure A.19** Specimen No.CCS-PWS-TI-3.
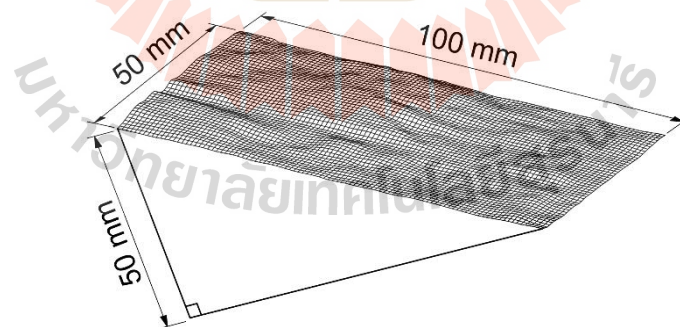
**Figure A.20** Specimen No.CCS-PWS-TI-4.
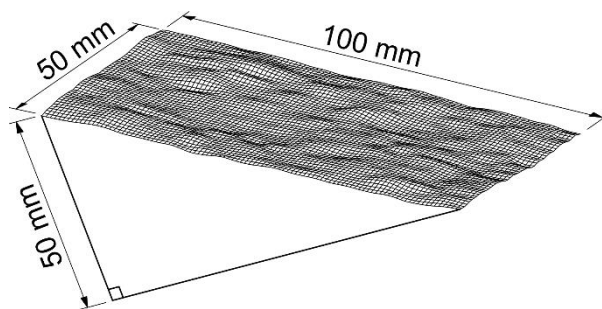
Figure A.21 Specimen No.CCS-PWS-TI-5.
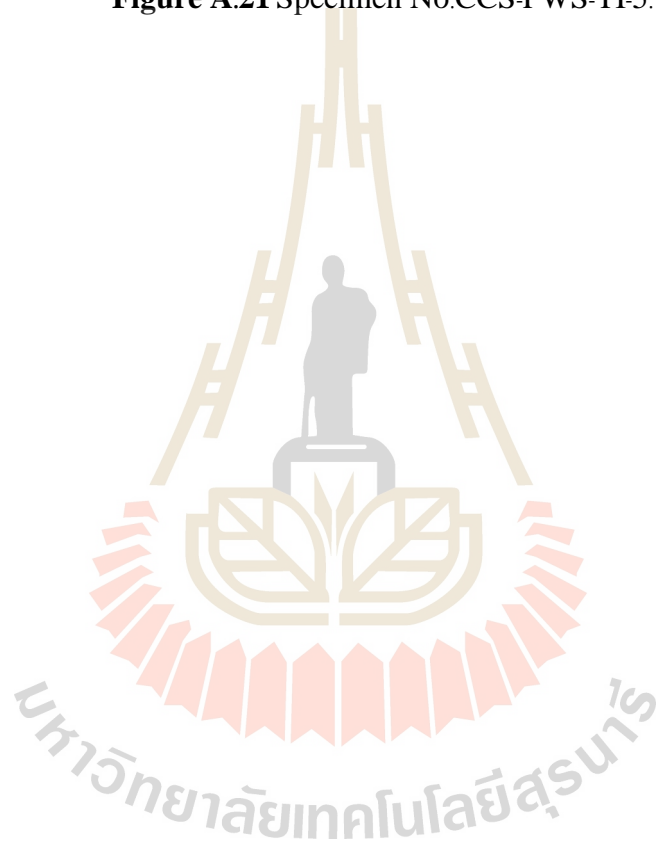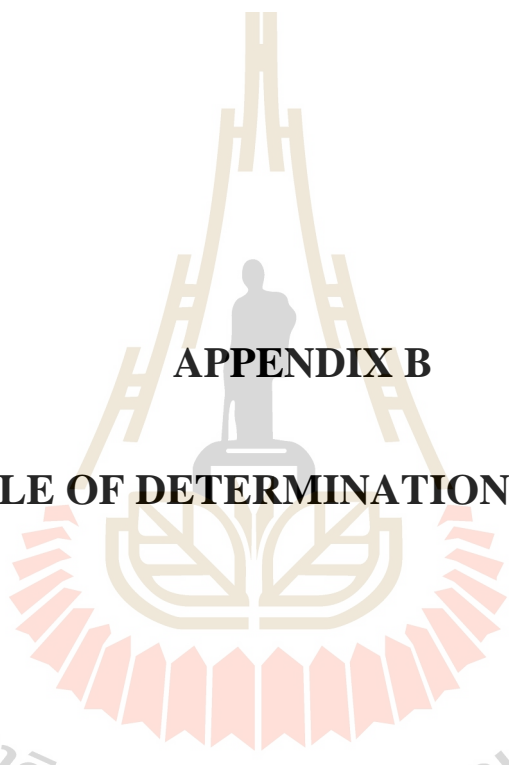
APPENDIX B

EXAMPLE OF DETERMINATION JRC VALUE
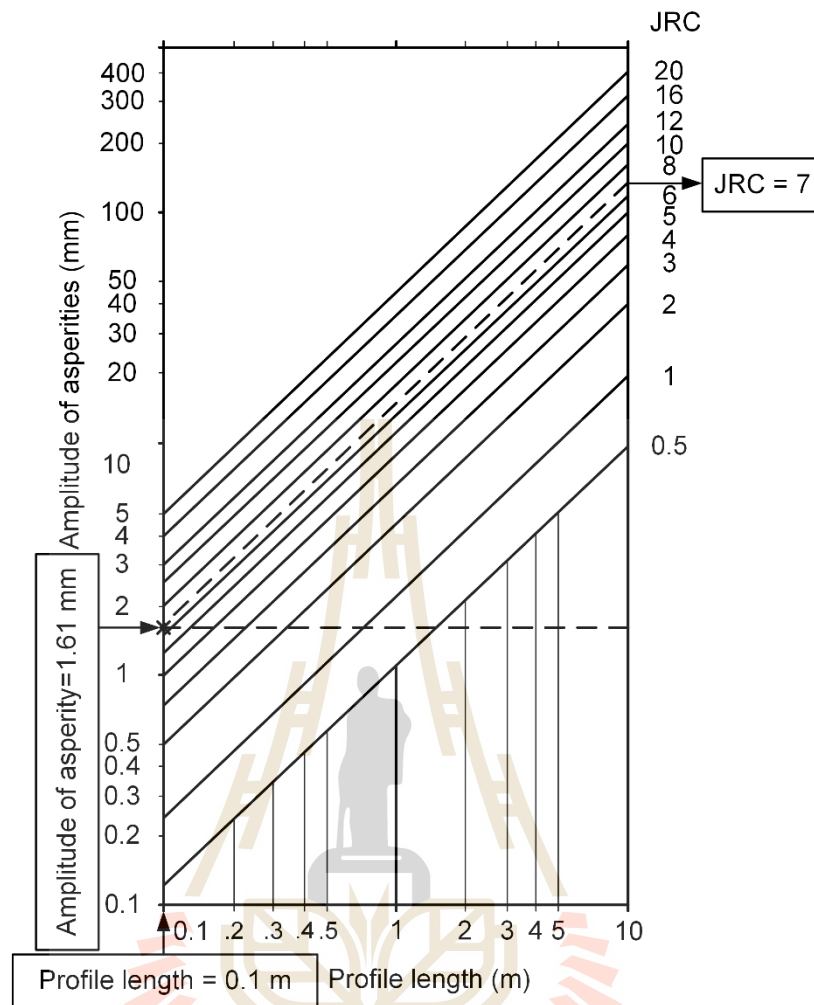
Figure B.1 Determination of JRC value of rough fracture (Modified from Barton, 1982).

The specimen No. CMS-PWS-TI-4 provides the measured amplitude of asperity of 1.61 mm. The measurement of the laser-scanned profile is detected along the profile length of 0.1 m. The JRC value of the rough fracture obtained from the Barton's chart equals to 7.

BIOGRAPHY

Mr. Pakpoom Naphudsa was born on December 28th, 1987 in Nakhon Ratchasima, Thailand. He received his Bachelor's Degree in Engineering (Geotechnology) from Suranaree University of Technology in 2011. For his post-graduate, he continued to study with a Master's degree in the Geological Engineering Program, Institute of Engineering, Suranaree university of Technology. During graduation, 2012-2014, he was a part time worker in position of Research Assistant at the Geomechanics Research Unit, Institute of Engineering, Suranaree University of Technology. He achieved his Master's degree in Engineering (Geotechnology) in 2014. He had then worked as an Engineering Geologist at Right tunnelling Co.,Ltd. for 2 years, involving in two major projects: Mae Saloum reservoir project in Chiang Mai, Thailand and Xe Pian-Xe Namnoy hydropower project in Attapeu, Laos.